machines

MDPI

Article

Attempts at Pseudo-Inverse Vibro-Acoustics by Means of SLDV-Based Full-Field Mobilities

Alessandro Zanarini

Dynamics & Vibrations of Machines, DIN – Department of Industrial Engineering, University of Bologna, Viale del Risorgimento 2, 40136 Bologna, Italy; a.zanarini@unibo.it

Abstract: Lightweight components can have structural integrity and reliability concerns, coming from dynamic airborne pressure fields. Hardly tuned numerical structural models may enter into vibro-acoustic simulations of the pressure fields radiated by vibrating plates, potentially masking the forecast of severe outputs. Instead, this paper proposes – for the direct and inverse vibro-acoustic approaches – to characterise the broad frequency band structural dynamics of radiating surfaces by means of experiment-based full-field contactless techniques, with increased spatial resolution, but without the inertia-related distortions of traditional measurement transducers. The SLDV-based *mobilities* bring the real-life behaviour of the component into the vibro-acoustic simulations, with the actual realisation-related complete structural dynamics and broad frequency band excitation. The paper aims at assessing the procedure for the estimation, in the whole spectrum, of the airborne force, which can be transmitted by an airborne pressure field to known structural locations. The simulation tools revisit the simple Rayleigh integral approximation of sound radiation from a vibrating surface, a real thin flat plate, describable by SLDV-based *complex-valued* full-field mobilities. Airborne pressure fields and excitation forces concern the early attempts of direct and pseudo-inverse vibro-acoustics. Details, examples and considerations about the whole procedures are thoroughly provided: on the simulation of the vibro-acoustic transfer matrix and of the radiated sound pressures with given excitation forces; on the retrieval of the airborne forces in restraining locations, together with the assessment of the numerical precision of the retrieving procedure.

Keywords: full-field vibro-acoustic FRFs; Rayleigh integral approximation; pseudo-inverse full-field vibro-acoustics; airborne pressure fields; induced airborne force estimation

Academic Editor: Fu-Cheng Wang

Received: 17 January 2025
Revised: 22 March 2025
Accepted: 31 March 2025
Published: 16 April 2025

Citation: Zanarini, A. Attempts at Pseudo-Inverse Vibro-Acoustics by Means of SLDV-Based Full-Field Mobilities. *Machines* **2025**, *13*, 324. https://doi.org/10.3390/machines13040324

1. Introduction

Prohibitive operational dynamic states can be reached from distributed dynamic loading, in the shape of airborne pressure fields. Lightweight components – especially in wind turbines for energy harvesting and in vehicle engineering for aircraft, space launchers, high speed trains and automotive shields – can decrease their forecast exercise life, when reduced by unexpected strain distributions from not fully understood airborne pressure fields. A possible reason for this partial lack of knowledge might be searched in the simplifications of the numerical models at the base of many NVH studies (see e.g. [1–11]). The latter simulate the sound radiation from vibrating parts by means of linear structural FEM, which might be improperly tuned for the specific manufactured realisation, or much simplified about non-linearities, specific damping-friction distributions and real boundary constraints. The real-life structural dynamics is strongly simplified also in fluid-structure interaction studies (see, in the frequency domain, [12–16]). In the literature mostly

focused on fluid motion (outside the target of this paper, but examples can be found in [17–25]), again the numerical structural model seems simplified, disregarding the real-life physical properties distribution and, in particular, the damping modelling, albeit relevant for the fluid-structure interactions and fluttering phenomena. Unfortunately, the most general modal modelling approach – based on *complex-valued eigensolutions* (see [26,27]) – and model updating/tuning do not seem to receive the deserved attention. The above suggested examples simplify the structure by a limited modal base from a linear FEM with proportional damping only, which means a truncated *real-valued* eigensystem. Broad frequency band experiment-based full-field optical FRFs (either *receptances* or *mobilities*) can be *complex-valued* alternatives to extract the most realistic linearisation of the real-life and complete structural dynamics directly from contactless testing, with great accuracy and enhanced spatial resolution, with no modal model identification nor truncation. This statement is based on the experience of the author, as later briefly sketched, in full-field measurement techniques – boosted by the TEFFMA project[1] – and on inspiring researches [28–31]. As proposed in this work, the *complex-valued* experiment-based *optical full-field mobilities* substitute any numerical modelling (e.g. by FEM) of the structural part, with no need of any model updating, material properties' and boundary conditions' guess.

Among the optical – therefore contactless, not distorting with sensors & cabling inertia – technologies, SLDV has permitted to add dofs and discrete spatial resolution in established NVH approaches in broad frequency ranges, but it can be better defined as *non-native* full-field measurement technique, due to its scanning nature. SLDV has therefore become a reference in contactless measurements for standing vibrations, but not for transients, not acquiring synchronously the whole mapping. SLDV is the full-field technology here adopted for the real-life *mobility* (velocities over forces) testing of the vibrating structural part. Instead, the techniques based on the sensing of photons across the whole sensor matrix can be called as optical *native* full-field measurements, or also *image-based*, with an even higher dofs' density and field-wise accuracy/continuity than that of SLDV, as proved extensively in [28–34], especially with stroboscopic ESPI. Although limited to standing vibrations in the frequency domain, ESPI can measure extremely detailed fields with a noise floor of the order of 50 nm and a ceiling of some μm, exploiting the interference phase maps and the precision of the constant wavelength of the coherent laser light, modulated up to several kHz in stroboscopic acquisitions. While quality-wise unsurpassed, for broad frequency band measurements ESPI has heavy drawbacks in the time consuming test, coherent lighting, recording size and environmental vibration insulation needs, hardly met outside a specific research laboratory. Another *native* full-field approach is that of DIC with good spatial detail (generally better than SLDV, but lower than ESPI) in the time histories of displacement maps. However, even with the usage of proper high-speed cameras, related to the frequency band of interest, DIC is generally more limited in the upper frequencies than SLDV, due to the different frequency domain amplification of displacements against velocities. But, with DIC, transients are easily acquired in the time domain if the on-board memory of the cameras allow long recordings; furthermore, the evaluation of multiple series of correlated displacements might be computationally intensive even nowadays. A relevant advantage of DIC systems is certainly their usage flexibility – therefore of increasing interest also in industrial environments – as some in-situ advanced applications have proved, as in [35–39]. Note how SLDV, Stroboscopic ESPI and Hi-speed DIC give *complex-valued* datasets in the frequency domain as in the TEFFMA project.

[1] A. Zanarini is the scientific proposer & experienced researcher in the project TEFFMA - Towards Experimental Full Field Modal Analysis, financed by the EC - Marie Curie FP7-PEOPLE-IEF-2011 PIEF-GA-2011-298543 grant, 1 February 2013 – 31 July 2015.

Concise notes about the author's experience in optical full-field measurements follow. The first hints of the TEFFMA project appeared in 2014[2], consolidated by more enhanced reports in 2015[3]. The first works were briefly gathered in [32]; in [33], instead, extended notes on the *full-field receptances' evaluation* followed; in [34] model updating exploited the full-field eigenshapes coming from the EFFMA. The quality of *native* (ESPI and DIC) full-field datasets – in broad frequency band dynamic testing – was underlined in [40]. Relevant achievements for rotational[4] and strain FRF high resolution maps were compared in [45]. The high quality strain FRF mapping further led to structural integrity[5] inquiries: that attention – to the dynamic responses and structural integrity from specific excitations – is here recalled in the assessment of the airborne distributed loading.

The author proved how – nowadays – full-field techniques already provide, even if not fully explored, clear improvements in EFFMA, but even more in advanced model updating, derivative calculations (rotational dofs, strains, stresses, risk index maps) and vibro-acoustics, thanks to the higher continuity and consistency of the fields in the datasets when compared to more traditional sensors. Therefore, a highly reliable experiment-based behavioural modelling of complex components – in their manufacturing and mounting state – may come from full-field optical *mobilities*, the latter retaining any modally dense structural dynamics and being able to deal with any dynamic signature of the excitation, under the linearity assumption. Section 2.1 recalls, therefore, the basis of experimental FRFs in the TEFFMA project, with a brief summary of the rig and testing procedures.

In Section 2.2 – inspired by the works in [1–9,11] – a full-field *complex-valued* re-elaboration of the Rayleigh integral approximation for the *direct* vibro-acoustic modelling is proposed. Indeed, the *vibro-acoustic transfer matrices* in this formulation are obtained by means of the *experiment-based full-field mobilities* from SLDV technique as frequency domain relations between the *excitation forces* on the structure and the *acoustic pressures* in the acoustic domain, similarly to the *experiment-based full-field receptances* already employed by the author in former works[6] about vibro-acoustics; no numerical structural model, of any type (e.g. FEM or boundary element modelling, wave-based or any functional expansion), is used. By using a specified excitation signature, the *direct* vibro-acoustic FRFs

[2] In Proceedings of the ISMA2014 including USD2014 - International Conference on Noise and Vibration Engineering, Leuven, Belgium, September 15-17, KU Leuven, 2014: see 'On the estimation of frequency response functions, dynamic rotational degrees of freedom and strain maps from different full field optical techniques' in *Dynamic testing: methods and instrumentation*; see 'On the role of spatial resolution in advanced vibration measurements for operational modal analysis and model updating' in *Operational modal analysis*.

[3] In Proceedings of the ICoEV2015 International Conference on Engineering Vibration, Ljubljana, Slovenia, September 7-10, Univ. Ljubljana & IFToMM, 2015, symposium *Full Field Measurements for Advanced Structural Dynamics*, see: 'Model updating from full field optical experimental datasets'; 'Comparative studies on full field FRFs estimation from competing optical instruments'; 'Accurate FRFs estimation of derivative quantities from different full field measuring technologies'; 'Full field experimental modelling in spectral approaches to fatigue predictions'.

[4] The reader is invited to explore in [26,27,41–44] the relevance that rotational dofs have in reliably modelling structures with high complexity and many components, although most times rotational dofs are completely disregarded because of their measurement burden.

[5] Specifically, a risk index was firstly introduced in On the defect tolerance by fatigue spectral methods based on full-field dynamic testing to locate the areas mostly exposed to failure in a part subjected to dynamic load, while in n the exploitation of multiple 3D full-field pulsed ESPI measurements in damage location assessment a damaged composite panel was tested in the same perspective. Recently, in [46], ESPI-based risk map variability was addressed by *real-valued* amplitude excitation signatures; the effect of the energy-injection location was investigated in [47]; both aspects were gathered in [48]. Although reduced – by interpolation in both spatial and frequency domains – to the more moderate resolutions of the SLDV references in the TEFFMA project, DIC-based full-field *receptances* were used instead in [49] for the risk index mapping. Instead, in [50] the *raw* datasets from DIC – with no numerical residuals due to the topology transforms and interpolations – boosted the risk index analyses; furthermore, the latter used *complex-valued* coloured noises for force signals, with potential randomness in the complex amplitude and phase.

[6] Specifically, in [51,52] the ESPI technique was used to explore the viability of the *direct* vibro-acoustic modelling, while in [53] the effect of errors on vibro-acoustics from SLDV-based mobilities was investigated; in [54] *raw* DIC-based were used without transforms' errors for pseudo-inverse vibro-acoustics.

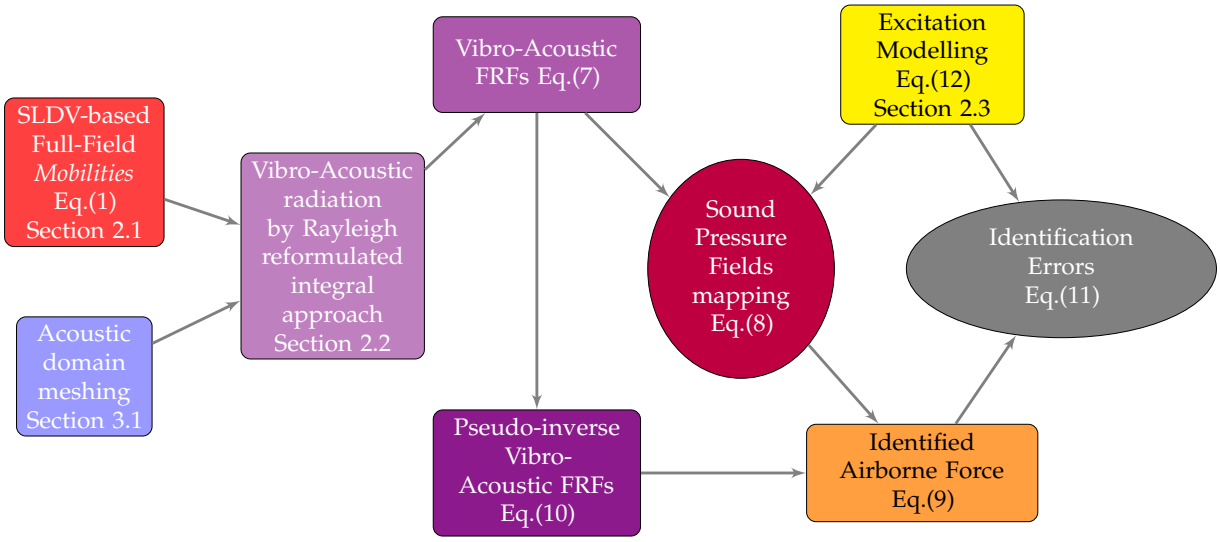

Figure 1. Main steps for the direct and pseudo-inverse airborne vibro-acoustics approaches.

can map the pressure field radiated by the vibrating plate. Another aim of this work is to assess the accuracy of an *inverse* vibro-acoustic approach in the interaction of airborne pressures with the structural dynamics. Therefore, expanding what already advanced in [55], a simplified *pseudo-inverse* airborne vibro-acoustics is developed in Section 2.2 by means of SLDV *full-field experiment-based mobilities* from the TEFFMA project. Starting from a known spectrum of the pressure field, the exerted force is reconstructed on the same excitation locations of the *direct* vibro-acoustic modelling. If the former pressure field was originated by a known force spectrum, the differences with the reconstructed force highlight the accuracy of the *pseudo-inverse* airborne vibro-acoustic procedure. With Section 2.3 a possible representation of broad frequency band forces is given by randomly contaminated coloured-noises, within the linearity assumption, as a realistic and enhanced *complex-valued* excitation broad frequency band spectrum that can fully promote the qualities of this *experiment-based full-field* approach.

The *direct* and *pseudo-inverse* vibro-acoustic approaches are simulated in Section 3, after notes on the computations and acoustic domain meshing. Specifically, the shapes of the *vibro-acoustic transfer matrices* are commented in relation to the SLDV *experiment-based full-field mobility maps*. Furthermore, by adopting specific excitation signatures, the radiated pressure fields are computed. These latter are feed back to the *pseudo-inverse* vibro-acoustic approach, after the comments on its FRFs, to assess the exerted airborne force on shaker head and the quality of the simplified identification procedure.

Section 4 gives a broader perspective on the results. Section 5 concludes by summarising the shown achievements. The reader can check in "Abbreviations" any nomenclature item that is used in the manuscript without explicit explanation.

2. Materials and Methods

The backbone of the experiment-based full-field vibro-acoustic approaches is sketched in Figure 1, as detailed in this Section. Details about the experiment-based modelling of lightweight structures by means of SLDV *mobilities* are given in Section 2.1, where the testing comes from the TEFFMA project. The *direct* and *pseudo-inverse* simplified vibro-acoustic approaches are presented in details in Section 2.2, where the Rayleigh integral approximation – of the relation between structural excitations and acoustic pressure fields –

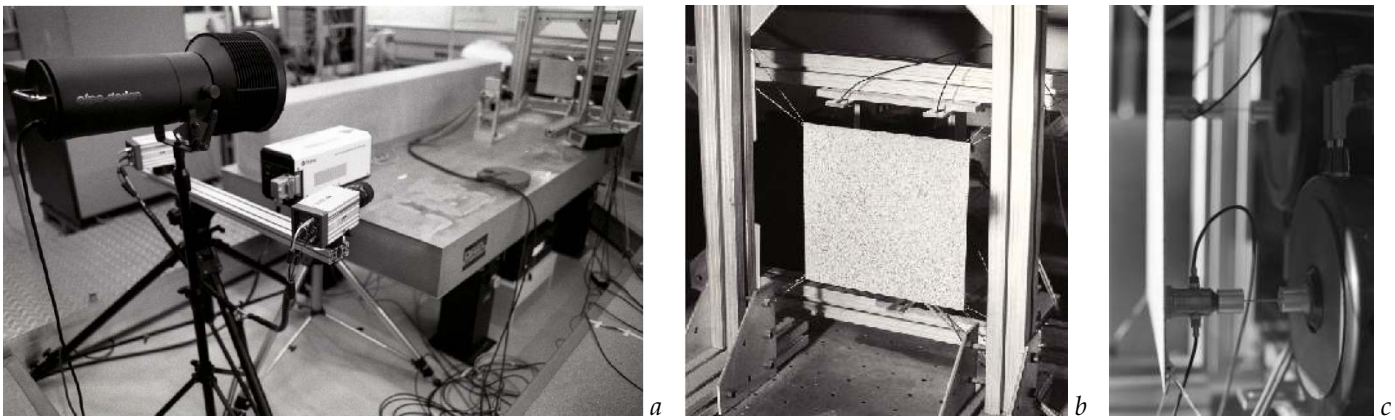

Figure 2. Full-field optical measurement instruments set-up in front of the specimen on the anti-vibration table with shakers on the backside: the instruments in (*a*) with SLDV head close to the border of the table, the restrained thin plate in (*b*) and the 2 shakers in (*c*).

is reformulated to take advantage of the *complex-valued* SLDV *mobilities*. In this perspective, a general modelling of the excitation is given in Section 2.3.

2.1. Full-Field SLDV Mobilities from the TEFFMA Project

At the Technische Universitaet Wien (Austria), the TEFFMA fundamental research project was led by the author. In it, SLDV was taken as the reference technology (albeit as *non-native*) in the comparisons among state-of-the-art optical *native*, or *image-based*, full-field approaches (Stroboscopic ESPI and Hi-speed DIC), in advanced structural dynamics and NVH studies. The TEFFMA project was based on the Post-doctoral Marie Curie Industry Host Fellowship project HPMI-CT-1999-00029 '*Speckle Interferometry for Industrial Needs*'[7] on ESPI-based testing, specifically for enhanced structural dynamics and fatigue life assessments, by means of spectral methods. During the TEFFMA project, as can be seen in Figure 2, the full-field measurement instruments (of SLDV, DIC and ESPI) were pivotal for all the activities; the test rig was assembled in a dedicated underground seismic-floor room, on an anti-vibration air-cushioning table, for the best insulation from environmental influences. These activities were favoured by the technicians of the mechanical & electronic workshop for customised tools. More detailed notes on the test campaign and on its achievements can be found in [33,34,40,45,54].

To make the unique comparisons in the TEFFMA project about the measurements for NVH and structural dynamics by the 3 full-field technologies, a common set-up was compulsory, but it only came after careful considerations on the limits of each approach. This unique set-up required a very fine tuning of even the smallest detail (revealed mostly by ESPI), but brought to a feasible performance overlapping of the different approaches. The same structural dynamics emerged in the frequency domain for ESPI and SLDV, but in the time domain for DIC. Although certainly not precisely super-imposable, the comparisons seemed certainly promising – from a qualitative point of view – already from each instrument software. Instead, to reach quantitative comparisons in the TEFFMA project – not here of specific interest – accurate topology transforms were implemented in the custom processing code, in order to have all the 3 different techniques' datasets cast on the same physical (geometry and frequency, as noted in the 2D graphs) references.

[7] It was held at Dantec Ettemeyer GmbH, Ulm, Germany. In particular, for the main achievements, see: 'Full field ESPI measurements on a plate: challenging experimental modal analysis', in: Proceedings of the XXV IMAC, Orlando (FL) USA, Feb 19-22, SEM, 2007; 'Fatigue life assessment by means of full field ESPI vibration measurements' in: P. Sas (Ed.), Proceedings of the ISMA2008 Conference, September 15-17, Leuven (Belgium); 'Full field ESPI vibration measurements to predict fatigue behaviour', in: Proceedings of the IMECE2008 ASME International Mechanical Engineering Congress and Exposition, October 31- November 6, Boston (MA), USA.

2.1.1. Characterisation of the Structural Dynamics by Means of *Full-Field Mobilities*

The *mobility* matrix $\boldsymbol{H_v}(\omega)$ follows the formulation for the H1 estimator - noise only in the outputs - found in [26,27]: it is estimated as the spectral relation between multi-output velocities and multi-input forces. In this full-field extension, the inputs are just 2 shakers, while *thousands* (2907) of responses are acquired on the whole surface of interest. The structural domain is represented by the vibrating surface S of the plate, whose *q-th* point has global 3D coordinates $\boldsymbol{q}_q$, while $\boldsymbol{q}$ represents all the field coordinates of the active structural domain. Each element of the *mobility* matrix $\boldsymbol{H_v}(\omega)$ can be expressed, in the *complex-valued* representation of the frequency domain, as:

$$H_{v_{qf}}(\omega) = \frac{\sum_{m=1}^{N} S^m_{\dot{X}_q F_f}(\omega)}{\sum_{m=1}^{N} S^m_{F_f F_f}(\omega)} \in \mathbb{C} \tag{1}$$

where $\dot{X}_q$ is the *output velocity* at q-th dof induced by the *input force* F_f at f-th dof, while $S^m_{\dot{X}_q F_f}(\omega)$ is the m-th cross-power spectral density between input and output, $S^m_{F_f F_f}(\omega)$ is the m-th auto-power spectral density of the input, evaluated in N repetitions.

2.1.2. Brief Notes About the Tested Plate in the TEFFMA Project

To avoid any confusion of static deformations with dynamic ODSs, a flat pristine thin aluminum rectangular plate – with external dimensions of 250 × 236 × 1.5 mm – was chosen as the specimen. The latter, to restrain any dangerous rigid-body movement for the ESPI technique, was fixed by wires to the rigid frame – bolted on the air-spring optical table – in Figures 2*a*, *b*. According to DIC requirements, a noise patter of random black & white droplets was sprayed on the plate face towards the instruments. The plate was excited orthogonally, from its back side, by the two properly positioned shakers of Figure 2*c*. The force signal – from the impedance heads at each shaker-structure interface – was recorded, for the estimation of the *mobility* FRFs $\boldsymbol{H_v}(\omega)$ in Equation (1). Stroboscopic ESPI-based measurements – in their phase-shifting procedures [56] – required shakers as controllable excitations, but the latter were fully compatible also with DIC and SLDV. The shakers were driven, one at a time, by an external sine-waveform generator in ESPI, on the contrary by LMS Test.Lab system in DIC and SLDV acquisitions.

2.1.3. Notes on the Processing of the *Full-Field Mobilities*

The formulation of Equation (1) permitted – in the TEFFMA project – the accurate estimation of *mobility FRF* maps from SLDV, and, similarly in [33], of *full-field receptances* for ESPI and DIC. Especially in ESPI datasets, the enhanced consistency and continuity of the spatial data in the sensed structural dynamics was appreciated, with remarkably clean ODSs, sharp nodal lines, and high-quality *Coherences* (see [26,27]). Each of the SLDV-based datasets – from the two shakers, differently positioned on the structure – retains N_q=2907 dofs (N_q= 57 × 51, about 4.39-4.64 mm grid spacing in the structural domain). Each dataset contains 1285 frequency lines, detached by a frequency space of 0.78125 Hz; the frequency range is limited to [20-1024] Hz, the lower end as imposed by ESPI technique. The number of averages is N=50.

SLDV-based datasets are here employed in their *raw* and undistorted estimations, with no down-sampling nor interpolations, thanks to unneeded topology transforms. Instead, if cast to the SLDV references, the higher spatial resolution *image*-based techniques of the TEFFMA project (DIC & ESPI) are forced to contain additional computational noise – albeit very limited in the customised routines – from the topology transforms.

2.2. Simplified Formulation for Direct and Pseudo-Inverse Vibro-Acoustics

At the core of a simplified vibro-acoustics is the relation between the structural motion – induced by excitation forces on the vibrating surface – and the radiated pressures in the facing medium. The latter definition pertains the here called *direct* vibro-acoustics, whereas by *inverse* vibro-acoustics the relation, between medium-borne pressure fields and induced forces on specific structural locations, is addressed.

The structural domain was already described and modelled in Section 2.1. The acoustic domain is here called A and its *a-th* point has global 3D coordinates $\boldsymbol{a}_a$, while $\boldsymbol{a}$ contains the whole field coordinates. Joining the results in literature [4,7,8,11,57] for propagating pressure waves, the sound pressure $p(\boldsymbol{a}_a, \omega)$ – output in $\boldsymbol{a}_a$, by a vibrating surface – can be defined in the frequency domain from the Helmholtz equation as:

$$p(\boldsymbol{a}_a, \omega) = 2i\omega\rho_0 \int_S v_n(\boldsymbol{q}_q, \omega) G(r_{aq}, \omega) dS_q \in \mathbb{C}, \qquad G(r_{aq}, \omega) = \frac{e^{-ikr_{aq}}}{4\pi r_{aq}} = \frac{e^{-i\omega r_{aq}/c_0}}{4\pi r_{aq}} \in \mathbb{C}, \tag{2}$$

where i is the imaginary unit, ρ_0 is the medium (air) density, $v_n(\boldsymbol{q}_q, \omega)$ is the normal (out-of-plane) velocity of the infinitesimal vibrating surface dS_q located in the $\boldsymbol{q}_q$ global coordinate, $k = \omega/c_0 = 2\pi/\lambda$ is the wavenumber in the Helmholtz equation (c_0 is the speed of sound at rest in the medium, λ is the acoustic wavelength), $r_{aq} = \|\boldsymbol{r}_{aq}\|$ is the norm of the distance $\boldsymbol{r}_{aq} = \boldsymbol{a}_a - \boldsymbol{q}_q$ between the points in the two domains, and $G(r_{aq}, \omega)$ is the free-space Green's function as described on the right of Equation (2).

2.2.1. Sound Pressures in a *Direct* Formulation of Vibro-Acoustics by *Full-Field Mobilities*

The *mobilities* of Equation (1) can be combined with the dynamic signature $\boldsymbol{F}_f(\omega)$ of the excitation (later modelled in Section 2.3) to obtain the *out-of-plane* velocities of the vibrating surface S. By using only the projection towards the surface normal, it yields:

$$\boldsymbol{v}_n(\boldsymbol{q}, \omega) = \boldsymbol{H}_{\boldsymbol{v}_n \boldsymbol{q} f}(\omega) \cdot \boldsymbol{F}_f(\omega) \in \mathbb{C}, \tag{3}$$

where the *mobility FRFs* $\boldsymbol{H}_{\boldsymbol{v}_{n_{qf}}}(\omega)$ is of size $N_q \times N_f$, N_q being the number of the outputs and N_f of the force inputs $\boldsymbol{F}_f(\omega)$.

The Rayleigh integral approximation of the Helmholtz equation works as substituting the integral of Equation (2) by the sum of the N_q discrete contributions ΔS_q of the pumping surface S around the structural mesh points, discretised as $S \approx \sum_q \Delta S_q$. By revisiting the Rayleigh integral approximation with the achievements of the FRF formulation of Equation (3), Equation (2) yields:

$$p(\boldsymbol{a}_a, \omega) \approx 2i\omega\rho_0 \sum_q^{N_q} \boldsymbol{H}_{\boldsymbol{v}_{n_{qf}}}(\omega) \boldsymbol{F}_f(\omega) G_{aq}(r_{aq}, \omega) \Delta S_q \in \mathbb{C}, \tag{4}$$

with $\boldsymbol{H}_{\boldsymbol{v}_{n_{qf}}}(\omega)$, $\boldsymbol{F}_f(\omega)$ and $G_{aq}(r_{aq}, \omega)$ as *complex-valued* discrete quantities.

$G_{aq}(r_{aq}, \omega)$ and ΔS_q are direct function of the discretisation of both domains, specifically subdivided in N_a discrete points in the acoustic domain and of the N_q points on the vibrating surface. $G_{aq}(r_{aq}, \omega)$ and ΔS_q can therefore contribute to define a *complex-valued diffusion matrix* $\boldsymbol{T}_{\boldsymbol{aq}}(\omega)$, sized $N_a \times N_q$, with each element composed by:

$$T_{aq}(\omega) = 2i\omega\rho_0 G_{aq}(r_{aq}, \omega) \Delta S_q. \tag{5}$$

Equation (4) can be algebraically rearranged as:

$$p(\boldsymbol{a}_a, \omega) \approx \boldsymbol{T}_{\boldsymbol{aq}}(\omega) \boldsymbol{H}_{\boldsymbol{v}_{n_{qf}}}(\omega) \boldsymbol{F}_f(\omega) \in \mathbb{C}. \tag{6}$$

Contrary to the *acoustic transfer vectors* (ATVs) in [5,58,59] between sound pressures and surface velocities, a *vibro-acoustic transfer matrix* $\boldsymbol{V_{af}}(\omega)$, sized $N_a \times N_f$, can be defined between *acoustic pressures* and *excitation forces* as:

$$\boldsymbol{V_{af}}(\omega) = \boldsymbol{T_{aq}}(\omega) \cdot \boldsymbol{H_{v_{nqf}}}(\omega) \in \mathbb{C}. \tag{7}$$

Therefore, Equation (6) can be easily compacted in:

$$p(\boldsymbol{a_a}, \omega) \approx \boldsymbol{V}_{af}(\omega)\boldsymbol{F}_f(\omega) \in \mathbb{C}. \tag{8}$$

Equation (8) is the pivot of the *direct* vibro-acoustic formulation here proposed, since it is able to map each sound pressure field, as the excitation varies, while the structural dynamics in the *mobilities* and the acoustic mesh do not change.

2.2.2. Induced Forces in a *Pseudo-Inverse* Formulation of Vibro-Acoustics by *Full-Field Mobilities*

The *direct* reformulation in Equation (8) of the Rayleigh integral approximation by the use of *mobilities* can be seen in the reverse way of an *inverse* formulation. The latter starts from known *complex-valued* pressure fields $\hat{\boldsymbol{p}}(\boldsymbol{a_a}, \omega)$ and aims at reconstructing the forces $\hat{\boldsymbol{F}}_f(\omega)$ induced in the structural locations of the *direct* problem's excitations, similarly to what found in [57,60–66], but knowing exactly the points. At the core of the *inverse* formulation stays the *pseudo-inversion* of the *vibro-acoustic transfer matrix* $\boldsymbol{V_{af}}(\omega)$ in Equation (7). Therefore, once the pressure field $\hat{\boldsymbol{p}}(\boldsymbol{a_a}, \omega) \in \mathbb{C}$ is used as the acoustic excitation, the forces $\hat{\boldsymbol{F}}_f(\omega)$ at the shakers' heads can be retrieved by:

$$\hat{\boldsymbol{F}}_f(\omega) \approx \boldsymbol{V}^+_{\boldsymbol{fa}}(\omega)\hat{\boldsymbol{p}}(\boldsymbol{a_a}, \omega) \in \mathbb{C}, \tag{9}$$

where $\boldsymbol{V}^+_{\boldsymbol{fa}}(\omega)$ is the *pseudo-inverse* of the *vibro-acoustic transfer matrix* $\boldsymbol{V_{af}}(\omega)$, sized $N_f \times N_a$, definable as *acoustic-vibrational FRF matrix* between the *acoustic pressures* in the medium and the *forces* on the structure – retaining its dynamics – and defined by:

$$\boldsymbol{V}^+_{\boldsymbol{fa}}(\omega) = [\boldsymbol{V}^H_{\boldsymbol{fa}}(\omega)\boldsymbol{V_{af}}(\omega)]^{-1}\boldsymbol{V}^H_{\boldsymbol{fa}}(\omega) \in \mathbb{C}, \tag{10}$$

$()^H$ being the Hermitian operator. Note that the internal inversion in Equation (10) is operated on the *complex-valued* kernel, sized only $N_f \times N_f$, which dramatically simplifies the *pseudo-inversion* when N_f is very small, like here with $N_f = 1$ with only one shaker at a time.

In order to assess the quality of the force retrieval procedure of Equation (9), an error function $\boldsymbol{Err}_{\boldsymbol{F}_f}(\omega) \in \mathbb{C}$ can be defined. It can be based on the difference between the original forces $\boldsymbol{F}_f(\omega)$ that generated the pressure fields $\boldsymbol{p}(\boldsymbol{a_a}, \omega)$ in Equation (8), later fed back – $\hat{\boldsymbol{p}}(\boldsymbol{a_a}, \omega) \equiv \boldsymbol{p}(\boldsymbol{a_a}, \omega)$ – to the acoustic excitation fields $\hat{\boldsymbol{p}}(\boldsymbol{a_a}, \omega)$ in the retrieval of medium-borne forces on the structure $\hat{\boldsymbol{F}}_f(\omega)$ of Equation (9), simply by:

$$\boldsymbol{Err}_{\boldsymbol{F}_f}(\omega) = \boldsymbol{F}_f(\omega) - \hat{\boldsymbol{F}}_f(\omega) \in \mathbb{C}. \tag{11}$$

2.3. Simple Broad Frequency Band Modelling of the Excitation Forces

The strength of this experimental *mobilities*-based approach comes from its avoiding simplifications of the linear responses of the real structure in a broad frequency range. Therefore, the modelled excitations must be defined in the same manner, same frequency domain and *complex-valued* nature. *Coloured noises* can generally represent the frequency domain deployment of broad band signals, with a definition in the whole range. The general shape of the *coloured noises* depends on the amplitude modulator parameter α, with

$\alpha \in [-2, 2]$ defining the *noise colour* ($\alpha = -2$ for *violet noise* as in Figures 10, 16 and 21; $\alpha = -1$ for *blue noise* as in Figures 8, 14 and 19; $\alpha = 0$ for *white noise* as in Figures 6, 12 and 17; $\alpha = 1$ for *pink noise* as in Figures 7, 13 and 18; and $\alpha = 2$ for *red noise* as in Figures 9, 15 and 20). Among all of them, the *white noise* keeps an even treatment of the amplitudes in all the frequency lines of the spectrum, to which some randomness might be added to better represent reality. Furthermore, proper phasing can be also added, with the same considerations about randomness. The other variances give more emphasis to the lower part of the spectral lines when $\alpha > 0$; instead, with $\alpha < 0$, more predominance is given to the higher frequency components of the spectra.

Complex-Valued Coloured Noise with *Random Amplitude* and *Phase* Variations

In order to appreciate the contribution of *experiment-based full-field mobilities*, thanks to their *complex-valued* representation of the real-life structural dynamics, different excitation signatures for $F(\omega) \in \mathbb{C}$ components can be discussed in the general formulation here proposed. The type of signal that better describes what can be generally acquired for forces in any real testing – with generically varied *complex-valued spectrum* – is that of a *complex-valued coloured noise* excitation, therefore with variable *complex amplitude* and *phase* in a fully populated broad frequency band, potentially *with random variations* in the *amplitude* & *phase*. Only the *linearity* – between forces and structural responses – needs to be respected. Here labelled as "*rap*", which stands for random variations in the modulated amplitude and sinusoidal phase, $F(\omega)$ can be defined as:

$$F(\omega) = \frac{F_{0_r}}{\omega^{\alpha}} e^{i\theta_r(\omega)} \in \mathbb{C}, \tag{12}$$

with $F_{0_r} = F_0(1 + \beta_{F_0}(Rand_{F_0} - 0.5))$, $\theta_r(\omega) = \theta(\omega)(1 + \beta_\theta(Rand_\theta - 0.5))$ with $\theta(\omega)$ as the chosen phase function, contaminated by amplitude & phase random variations. In Equation (12) the other quantities are: $F_0 \in \mathbb{R}$, the reference amplitude; $\beta_{F_0} \in \mathbb{R}$, $0 \leq \beta_{F_0} \leq 1$, the level of randomness in the amplitude; $Rand_{F_0}$, or $Rand_\theta$, a function returning a pseudo-random number in the range 0 to 1, respectively for the amplitudes or for the phases; $\theta(\omega) = S_0 sin(\pi N_p(\omega - \omega_0)/\Delta\omega + \theta_0)$, a selected phase function; S_0, the sinusoidal phase range multiplier; N_p, the number of half cycles of the phase in the range; ω_0, the starting frequency; $\Delta\omega$, the frequency range; θ_0, a reference phase; β_θ, the level of randomness in the phase. For all the examples here provided, the following inputs were taken: $F_0 = 0.075$ N, $S_0 = 0.75$ rad, $N_p = 6.5$, $\theta_0 = \pi/4$ rad, $\beta_{F_0} = 0.125$, $\beta_\theta = 0.25$, with the respective quantities explained above.

Equation (12) clearly appears much more adherent to real-life excitations, as found in any random-noise shaker testing, with a generically varied *complex-valued* spectrum. In the procedures here proposed, based on *full-field mobilities* from testing, therefore, no limitations nor assumptions are imposed on the excitations, except the respect of the linearity of the structural responses with the shaking forces.

3. Results

This section is devoted to putting together the real-life testinThis Section is devoted to put together the real-life testing of Section 2.1 – by examples of *full-field* SLDV-based *mobilities* in Equation (1) – with the acoustic radiation simulations formulated in Section 2.2. In particular, as summarised respectively in Tables 1 & 2, attention is given to the *vibro-acoustic transfer matrix* $\boldsymbol{V_{af}}(\omega)$ in Equation (7) to simulate the *acoustic pressure* $p(\boldsymbol{a}_a, \omega)$ in Equation (8), thanks to the excitation signatures proposed in Section 2.3. Furthermore, as reported in Table 3, the *acoustic-vibrational FRF matrix* $\boldsymbol{V}^+_{\boldsymbol{fa}}(\omega)$ of Equation (10) is calculated, in order to estimate the airborne force in Equation (9) and related errors of Equation (11).

Table 1. Summary of the proposed examples of *vibro-acoustic transfer matrix*.

Section	Equation	Quantity	Structural Excitation	Acoustic Domain	Frequency Domain	Figure
3.2	(7)	$V_{aS_1}(\omega)$	S1, –	single dof [374]	[20-1024] Hz	3*a*
3.2	(7)	$V_{aS_2}(\omega)$	S2, –	single dof [374]	[20-1024] Hz	3*b*
3.2	(7)	$\boldsymbol{V}_{aS_1}(\omega)$	S1, –	whole mesh	121.1 Hz	4*a*
3.2	(7)	$\boldsymbol{V}_{aS_1}(\omega)$	S1, –	whole mesh	127.5 Hz	4*b*
3.2	(7)	$\boldsymbol{V}_{aS_1}(\omega)$	S1, –	whole mesh	250.0 Hz	4*c*
3.2	(7)	$\boldsymbol{V}_{aS_1}(\omega)$	S1, –	whole mesh	284.4 Hz	4*d*
3.2	(7)	$\boldsymbol{V}_{aS_1}(\omega)$	S1, –	whole mesh	335.9 Hz	4*e*
3.2	(7)	$\boldsymbol{V}_{aS_1}(\omega)$	S1, –	whole mesh	496.1 Hz	4*f*
3.2	(7)	$\boldsymbol{V}_{aS_1}(\omega)$	S1, –	whole mesh	754.7 Hz	4*g*
3.2	(7)	$\boldsymbol{V}_{aS_1}(\omega)$	S1, –	whole mesh	990.6 Hz	4*h*
3.2	(7)	$\boldsymbol{V}_{aS_2}(\omega)$	S2, –	whole mesh	121.1 Hz	5*a*
3.2	(7)	$\boldsymbol{V}_{aS_2}(\omega)$	S2, –	whole mesh	127.5 Hz	5*b*
3.2	(7)	$\boldsymbol{V}_{aS_2}(\omega)$	S2, –	whole mesh	250.0 Hz	5*c*
3.2	(7)	$\boldsymbol{V}_{aS_2}(\omega)$	S2, –	whole mesh	284.4 Hz	5*d*
3.2	(7)	$\boldsymbol{V}_{aS_2}(\omega)$	S2, –	whole mesh	335.9 Hz	5*e*
3.2	(7)	$\boldsymbol{V}_{aS_2}(\omega)$	S2, –	whole mesh	496.1 Hz	5*f*
3.2	(7)	$\boldsymbol{V}_{aS_2}(\omega)$	S2, –	whole mesh	754.7 Hz	5*g*
3.2	(7)	$\boldsymbol{V}_{aS_2}(\omega)$	S2, –	whole mesh	990.6 Hz	5*h*

Table 2. Summary of the proposed *sound pressure* results.

Section	Equation	Quantity	Structural Excitation	Acoustic Domain	Frequency Domain	Figure
3.3	(8)	$p(\boldsymbol{a}_a, \omega)$	S1, *white noise-rap*	single dof [374]	[20-1024] Hz	6*a*
3.3	(8)	$p(\boldsymbol{a}_a, \omega)$	S2, *white noise-rap*	single dof [374]	[20-1024] Hz	6*b*
3.3	(8)	$p(\boldsymbol{a}_a, \omega)$	S1, *pink noise-rap*	single dof [374]	[20-1024] Hz	7*a*
3.3	(8)	$p(\boldsymbol{a}_a, \omega)$	S2, *pink noise-rap*	single dof [374]	[20-1024] Hz	7*b*
3.3	(8)	$p(\boldsymbol{a}_a, \omega)$	S1, *blue noise-rap*	single dof [374]	[20-1024] Hz	8*a*
3.3	(8)	$p(\boldsymbol{a}_a, \omega)$	S2, *blue noise-rap*	single dof [374]	[20-1024] Hz	8*b*
3.3	(8)	$p(\boldsymbol{a}_a, \omega)$	S1, *red noise-rap*	single dof [374]	[20-1024] Hz	9*a*
3.3	(8)	$p(\boldsymbol{a}_a, \omega)$	S2, *red noise-rap*	single dof [374]	[20-1024] Hz	9*b*
3.3	(8)	$p(\boldsymbol{a}_a, \omega)$	S1, *violet noise-rap*	single dof [374]	[20-1024] Hz	10*a*
3.3	(8)	$p(\boldsymbol{a}_a, \omega)$	S2, *violet noise-rap*	single dof [374]	[20-1024] Hz	10*b*

The latter are useful for assessing the quality of the force retrieval procedure, with also its computational precision. All these results are accompanied by the related details and comments.

Some general notes about all the 2D frequency domain graphs are here given. At the top of each figure, generally three lines of coloured text are annotated. The first contains, on the left side, the frequency step and the corresponding value in Hertz, in dark yellow, linked to the vertical line in the graph, or cursor; at the centre, in magenta, the dof of inquiry is proposed before the name of the main function of the graph. The second line, on the right side, shows in blue the value of the main function at the cursor's abscissa, with related bracketed quantities; eventually, in the case of *complex amplitude* and *phase*, this information is split also to the third line. The third line can be instead taken, when only the *amplitude* of the functions is shown, by the description of the eventually added function and value at the cursor position, in black with left margin. The sketched functions, or *complex-valued* parts, are framed by grey lines, with the main functions' extremes and bracketed dimensions on the right side in grey text, while the frequency range is annotated in grey text at the very bottom of the frame. Another text line, at the very bottom, indicates the geometrical and frequency references (here both reporting SLDV), together with the used shaker in the specific structural dof, marking it with dark yellow, whereas the mute shaker is in dark grey. Inside the frame, the main function is drawn in pure blue, and the measurement technology (here SLDV) is recalled in blue text at the right of the frame. The dark yellow vertical cursor intercepts the main function in a point through which an horizontal light blue line is added

to show the reached main function value. If another function is superimposed – with its own ordinate quantities, scales and ranges annotated on the right of the frame – the chosen colour is pure black, but the value at the cursor position is only reported in the text above.

Some notes on the proposed maps of the figures follow to help the reader better understand the information they provide. First, the top-line text describes briefly the sketched function, followed by the indication of the active (in dark yellow text) and mute (in dark grey text) shakers, with corresponding structural dofs, also reported on the map by a big dot. For SLDV datasets, shaker 1 was in structural dof 2611, shaker 2 in structural dof 931. The third grey text line contains the frequency step and the corresponding value in Hertz. All the maps are 3D *complex-valued* fields, but projected with the same geometrical view and phasing angle to keep the comparisons viable. Therefore, the fourth text line says which *complex-valued* part is figured, while the fifth line gives the projecting phase angle. For the *mobility* ODS of the structural domain (positioned in front of the acoustic mesh to give a hint of the radiation source), blue tones are associated to the out-of-plane motion, giving brightest blue (rgb=[0,0,1]) to the maximal value of the velocity in the range, while giving darkest blue (rgb=[0,0,0], or pure black) to the lowest value in the range. Also the triangles of the maps, rendered by OpenGL primitives, are coloured accordingly with the colours of the defining points. Instead, for the acoustic mesh, grey tones are associated to the shown function, with pure white (rgb=[1,1,1]) in the maximum value, while pure black(rgb=[0,0,0]) is associated to the minimal value in the range. The ranges of the sketched vibro-acoustic function are drawn on the left side of each map, with the linearly varying grey tones and the extremes of the whole range. On each acoustic mesh, an inquiry acoustic dof is highlighted by a magenta big dot; its number (here 374) is written in the magenta text (sixth line) above the maps, not to be confused with the structural dofs of the shakers on the *mobility* ODS; the value of the function reached in the inquiry dof is reported in blue in the seventh text line, but also by a magenta dash in the side range bar.

Table 3. Summary of the proposed pseudo-inverse vibro-acoustic quantities: *acoustic-vibrational FRFs*, *estimated airborne forces* and *identification errors*.

Section	Equation	Quantity	Acoustic Domain, Excitation	Structural Domain	Frequency Domain	Figure
3.4	(10)	$V^{+}_{S_1 a}(\omega)$	single dof [374], –	S1	[20-1024] Hz	11*a*
3.4	(10)	$V^{+}_{S_2 a}(\omega)$	single dof [374], –	S2	[20-1024] Hz	11*b*
3.5	(9)	$\hat{F}_{S1}(\omega)$	whole mesh, *white noise-rap*	S1	[20-1024] Hz	12*a*
3.5	(11)	$Err_{F_{S1}}(\omega)$	whole mesh, *white noise-rap*	S1	[20-1024] Hz	12*b*
3.5	(9)	$\hat{F}_{S1}(\omega)$	whole mesh, *pink noise-rap*	S1	[20-1024] Hz	13*a*
3.5	(11)	$Err_{F_{S1}}(\omega)$	whole mesh, *pink noise-rap*	S1	[20-1024] Hz	13*b*
3.5	(9)	$\hat{F}_{S1}(\omega)$	whole mesh, *blue noise-rap*	S1	[20-1024] Hz	14*a*
3.5	(11)	$Err_{F_{S1}}(\omega)$	whole mesh, *blue noise-rap*	S1	[20-1024] Hz	14*b*
3.5	(9)	$\hat{F}_{S1}(\omega)$	whole mesh, *red noise-rap*	S1	[20-1024] Hz	15*a*
3.5	(11)	$Err_{F_{S1}}(\omega)$	whole mesh, *red noise-rap*	S1	[20-1024] Hz	15*b*
3.5	(9)	$\hat{F}_{S1}(\omega)$	whole mesh, *violet noise-rap*	S1	[20-1024] Hz	16*a*
3.5	(11)	$Err_{F_{S1}}(\omega)$	whole mesh, *violet noise-rap*	S1	[20-1024] Hz	16*b*
3.5	(9)	$\hat{F}_{S2}(\omega)$	whole mesh, *white noise-rap*	S2	[20-1024] Hz	17*a*
3.5	(11)	$Err_{F_{S2}}(\omega)$	whole mesh, *white noise-rap*	S2	[20-1024] Hz	17*b*
3.5	(9)	$\hat{F}_{S2}(\omega)$	whole mesh, *pink noise-rap*	S2	[20-1024] Hz	18*a*
3.5	(11)	$Err_{F_{S2}}(\omega)$	whole mesh, *pink noise-rap*	S2	[20-1024] Hz	18*b*
3.5	(9)	$\hat{F}_{S2}(\omega)$	whole mesh, *blue noise-rap*	S2	[20-1024] Hz	19*a*
3.5	(11)	$Err_{F_{S2}}(\omega)$	whole mesh, *blue noise-rap*	S2	[20-1024] Hz	19*b*
3.5	(9)	$\hat{F}_{S2}(\omega)$	whole mesh, *red noise-rap*	S2	[20-1024] Hz	20*a*
3.5	(11)	$Err_{F_{S2}}(\omega)$	whole mesh, *red noise-rap*	S2	[20-1024] Hz	20*b*
3.5	(9)	$\hat{F}_{S2}(\omega)$	whole mesh, *violet noise-rap*	S2	[20-1024] Hz	21*a*
3.5	(11)	$Err_{F_{S2}}(\omega)$	whole mesh, *violet noise-rap*	S2	[20-1024] Hz	21*b*

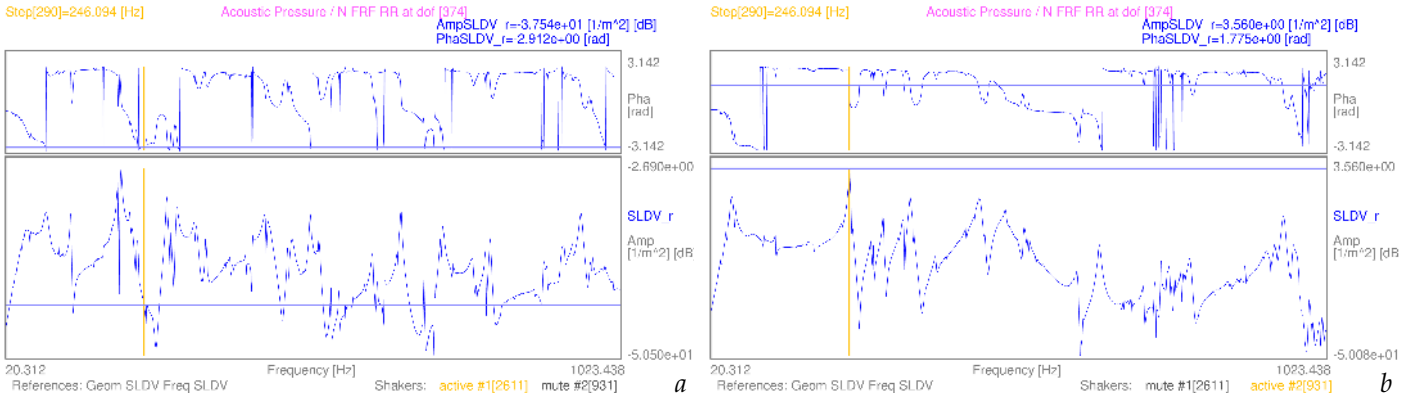

Figure 3. SLDV-based examples of *vibro-acoustic FRF* graphs in the frequency domain evaluated in acoustic dof 374, with excitation from shaker 1 in (*a*), from shaker 2 in (*b*).

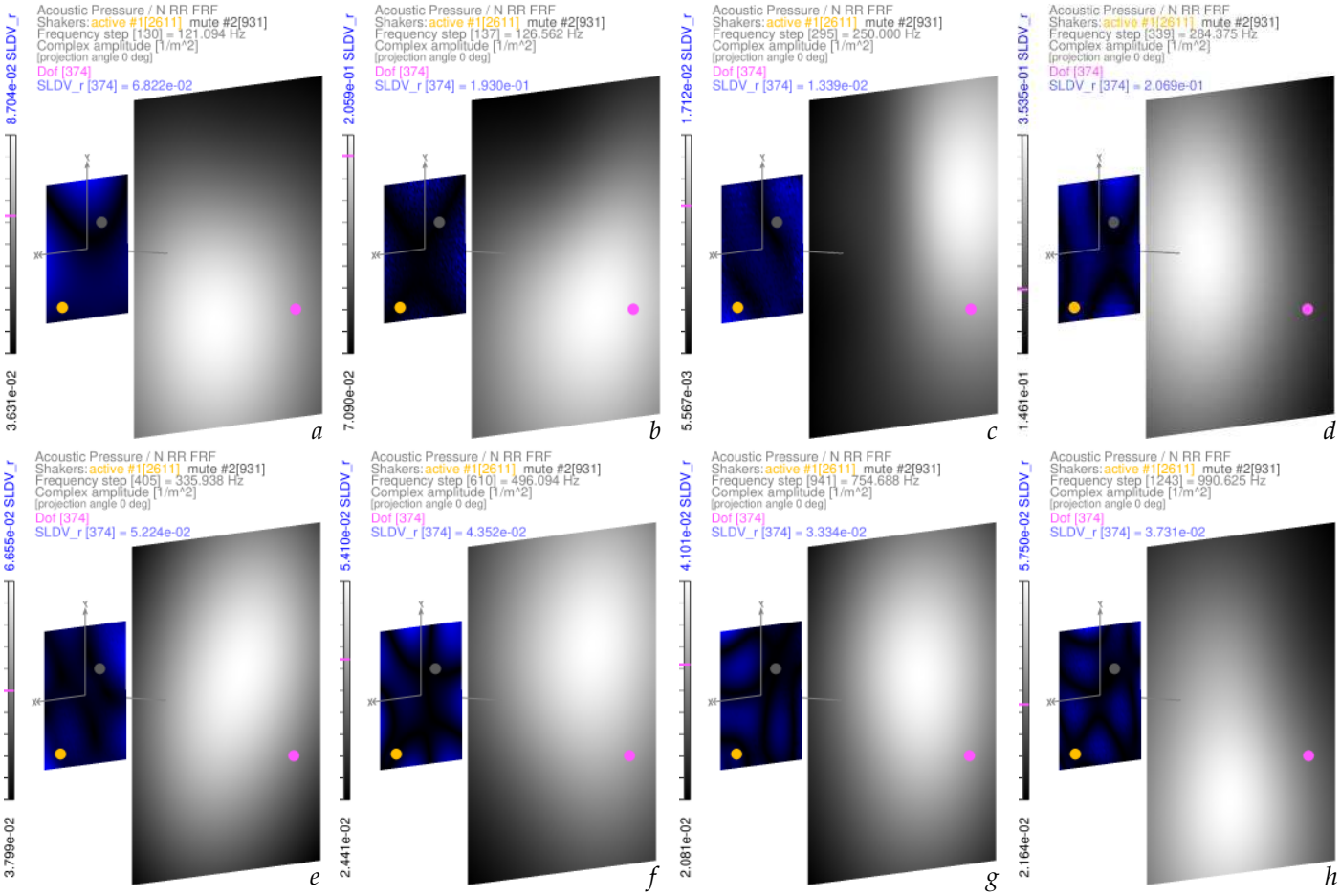

Figure 4. SLDV-based examples of *vibro-acoustic transfer matrix* mesh, with the highlighted (magenta) acoustic dof 374, excitation from shaker 1, in its *complex-valued* amplitude evaluated at different frequencies: 121 Hz in (*a*), 127 Hz in (*b*), 250 Hz in (*c*), 284 in (*d*), 336 Hz in (*e*), 496 Hz in (*f*), 755 Hz in (*g*), 991 Hz in (*h*).

3.1. Brief Notes on the Acoustic Domain Modelling

In all the simulations of the interaction between the structural domain – extensively defined in Section 2.1 – and the acoustic domain, the latter, among the many choices, is modelled as follows: a squared mesh, of size 0.5 m $\times$ 0.5 m, spatially sampled every 10 mm by 51 $\times$ 51 dofs (N_a=2601), distant 0.25 m from the vibrating plate, on which it is centred.

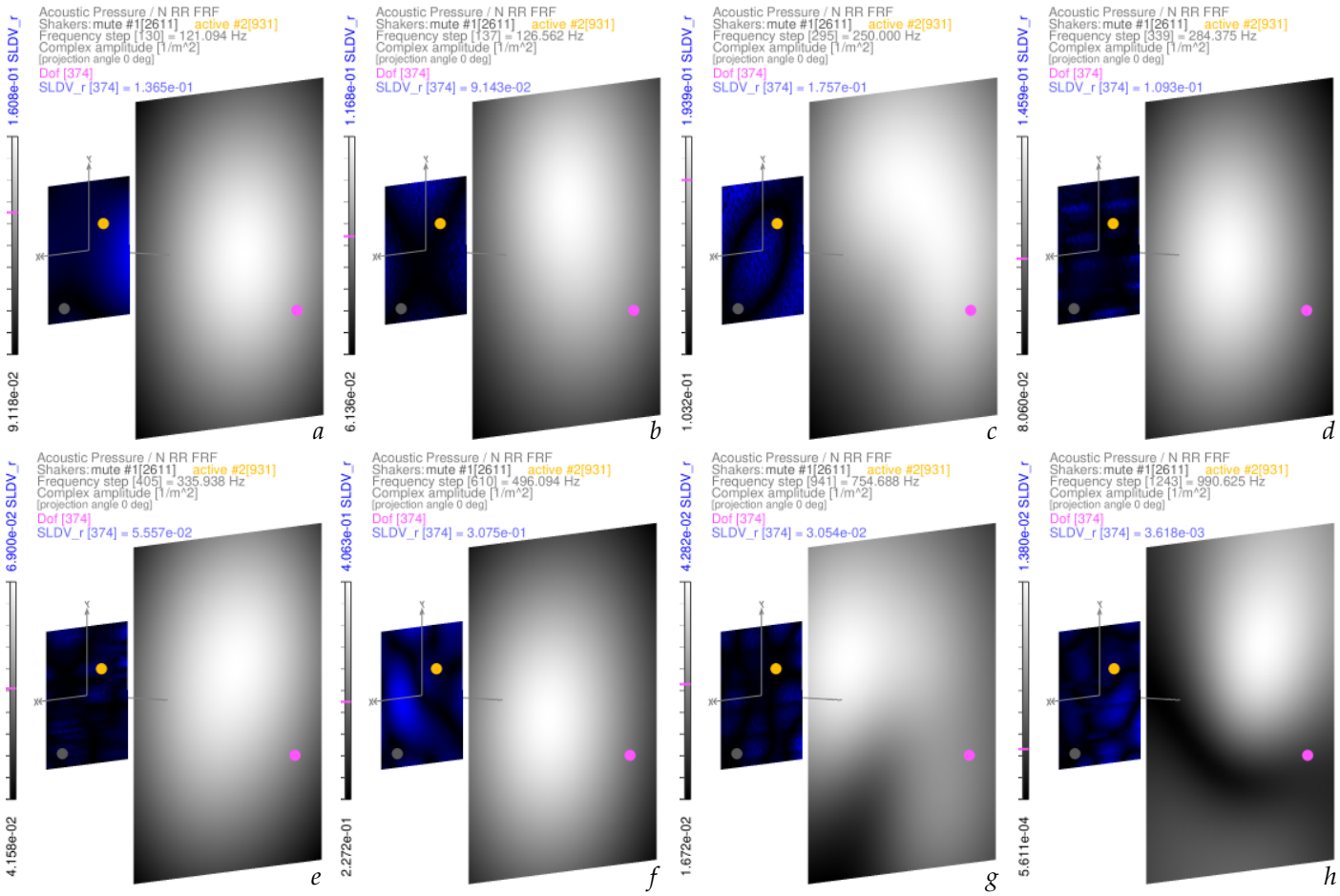

Figure 5. SLDV-based examples of *vibro-acoustic transfer matrix* mesh, with the highlighted (magenta) acoustic dof 374, excitation from shaker 2, in its *complex-valued* amplitude evaluated at different frequencies: 121 Hz in (*a*), 127 Hz in (*b*), 250 Hz in (*c*), 284 in (*d*), 336 Hz in (*e*), 496 Hz in (*f*), 755 Hz in (*g*), 991 Hz in (*h*).

During the TEFFMA testing, unfortunately, a precise recording of the ambient temperature was not made, therefore here the assumption of a likely room temperature of 15°C is made. This serves to obtain from [67] the medium data, matching the sensing of the structural dynamics in Section 2.1: the speed of sound c_0=340.27 m/s and the air density ρ_0=1.225 kg/m^3. For the sake of showing the potential of these *hybrid* vibro-acoustic simulations, the assumed values can be considered sufficiently realistic. Indeed, if testing the components for different air conditions[8], the structural testing should be run in a climate-chamber, to fully replicate the material behaviour in those conditions.

3.2. Vibro-Acoustic Transfer Matrices from Experiment-Based SLDV Mobilities

This section, by means of the formulation of Section 2.2, wants to highlight the high-quality results, in terms of field continuity and detail, of the *vibro-acoustic transfer matrix* $\boldsymbol{V}_{af}(\omega)$, as obtained from accurate *experiment-based SLDV mobilities* in optical testing, but without any numerical structural model, which instead might be hard to tune and give a limited representation of the real-life behaviour, especially regarding the damping distribu-

[8] Working on the information obtainable in [67,68], one can see how, at sea level, c_0 varies in the range of [315.77 – 351.88] m/s and ρ_0 in the range [1.4224 – 1.1455] kg/m^3 as the temperature rises from -25°C to +35°C. Furthermore, with the altitude c_0 flattens to about 295–300 m/s, while ρ_0 is more variable, in rising from the Troposphere (0–11 km) into the Tropopause (11-20 km), having a strongly variable range [1.225 (sea level, 15°C) – 0.3639 (11 km, -56.5°C) – 0.088 (20 km, -56.5°C)] kg/m^3.

tion, materials' characteristics, simplifications on the mounting/boundary conditions and dynamics truncation at higher frequencies.

In Figure 3 examples of the *vibro-acoustic transfer matrix* $\boldsymbol{V_{af}}(\omega)$ are reported as a frequency domain relation from shaker 1 (Figure 3*a*), or shaker 2 (Figure 3*b*), and acoustic dof 374, here selected in the squared acoustic mesh. It can be clearly seen how the data retain completely the *complex-valued* nature of the experiment-based full-field *mobilities*, especially in the damping around resonances and anti-resonances, or in the blending at any other frequency line. This type of results is hardly obtainable by synthetic structural models without a complete tuning or model updating, as in [34,43].

In Figures 4 and 5 the whole acoustic mesh of the *vibro-acoustic transfer matrix* is displayed in grey tones behind the estimated *mobility* matrix $\boldsymbol{H_{v_{nqf}}}(\omega)$ of the vibrating & radiating plate in blue tones at 121.1, 126.6, 250.0, 284.4, 335.9, 496.1, 754.7, 990.6 Hz, respectively, with the *complex-valued amplitudes* of both the structural and acoustic domains. Beside each tile, the range scale in grey tones allows to locate, by means of a magenta line, the level reached by the *vibro-acoustic transfer matrix* in the acoustic dof 374, which is the magenta dot, highlighted on the acoustic mesh. As anticipated, darker tones correspond linearly to the minimal values in the range, while full brightness pertains to the maximal values. Instead, the dark yellow dot on the vibrating plate ODS locates the active shaker, while the dark grey dot references the mute one.

In Figures 4 and 5 the evaluations of the *vibro-acoustic transfer matrix* $\boldsymbol{V_{af}}(\omega)$ are shown over the entire acoustic mesh, retaining the *complex-valued* relations and phase delays, coming from the *complex-valued mobility* matrix $\boldsymbol{H_{v_{nqf}}}(\omega)$, but blended in the *complex-valued* summation by Green's function. The distance of the acoustic mesh plays a relevant role in this blending, or averaging with fading effects, of the contributions[9] of specific areas on the vibrating plate. Indeed, due to the greater distance – between the acoustic mesh and the vibrating plate – here simulated, in the *complex amplitude* of Figures 4 and 5, the many discontinuities in the corresponding *mobility maps* are evened in a nearly constant field for the *vibro-acoustic transfer matrix*. The *complex-valued* mixing of the *diffusion matrix* $\boldsymbol{T_{aq}}(\omega)$ in Equation (7) blends the contribution of the *mobility maps* in an evened field. Therefore, as

[9] In particular, when the vibrating surface is at nearfield distance, it can reveal the proximity to specific nodal lines of the structural ODSs, especially at lower frequencies. The motion of the structural ODS in the extreme corners also seem to have some relevance here onto the far distance blending of the *vibro-acoustic transfer matrix*. Instead, as was shown in [53], at closer distances the structural ODS projects into the *vibro-acoustic transfer matrix* mesh with a much clearer reproduction of nodal lines' pattern. This was also manifest in [54], where the *complex amplitude* on the acoustic mesh mixes in a smoother field those components, coming from a more articulated pattern in the structural ODS.

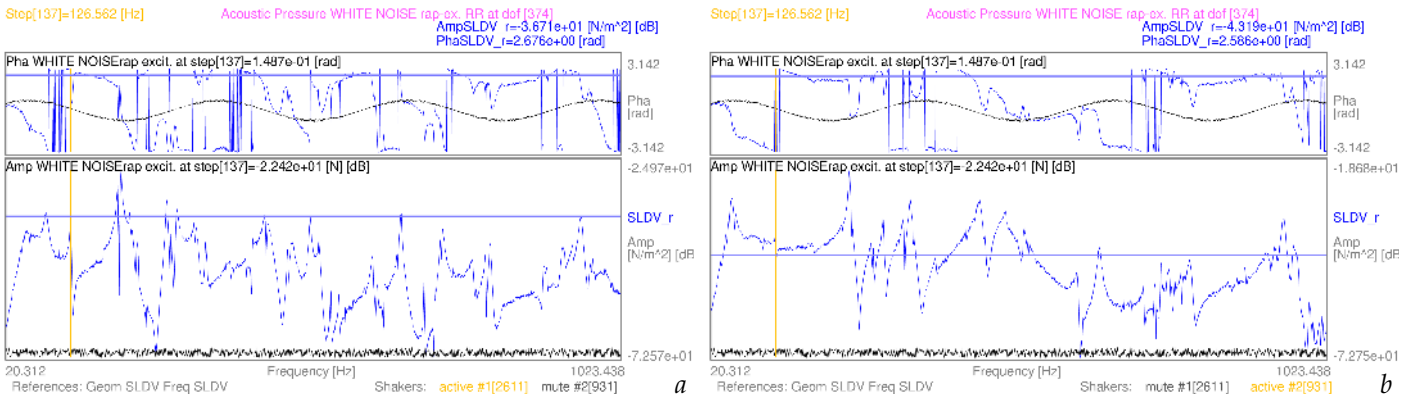

Figure 6. SLDV-based examples of *acoustic pressure complex-valued spectrum* graphs in the frequency domain evaluated in acoustic dof 374, from a *white noise-rap* excitation, by shaker 1 in (*a*), shaker 2 in (*b*).

the frequency rises, indeed more shape complexity pertains the *mobility* maps, as can be clearly seen in Figures 4*a*–*h* and in Figures 5*a*–*h* as well; but the resulting *complex-valued* blending in each point of the *vibro-acoustic transfer matrix* field, taking into account all the N_q=2907 contributions across the radiating surface, properly phased, has quite a different shape now, coming from the *complex-valued* summation, driven by Green's functions in Equations (4) and (7).

3.3. Acoustic Pressure Spectra from Experiment-Based SLDV Mobilities and Complex-Valued Forces

The full retention of the *complex-valued* nature of the *vibro-acoustic transfer matrix* is displayed together with the specific signatures of the excitations, e.g. as modelled in Section 2.3, for the deployment in the whole frequency domain here analysed ([20-1023] Hz). The display of the fields of *acoustic pressure* in the acoustic mesh is disregarded, because the modulation of any excitation's variant leads only to a scaling of the relative distribution in the *complex amplitudes*, shown for the *vibro-acoustic transfer matrix*, but with a specific phasing. Instead, the *complex-valued* spectra are here of major interest.

Compared to the shape of the *vibro-acoustic transfer matrix* shown in Figure 3, it is clear in Figure 6 how the *white noise-rap* excitation (in black) introduces a nearly constant – due to the limited randomness – *complex amplitude* scaling in the whole spectrum of the *acoustic pressure* (in blue) at dof 374, whereas the *phase* modifications appear stronger. Indeed, the slight randomness – of ±6.25% in the amplitudes – of the *white noise-rap* excitation,

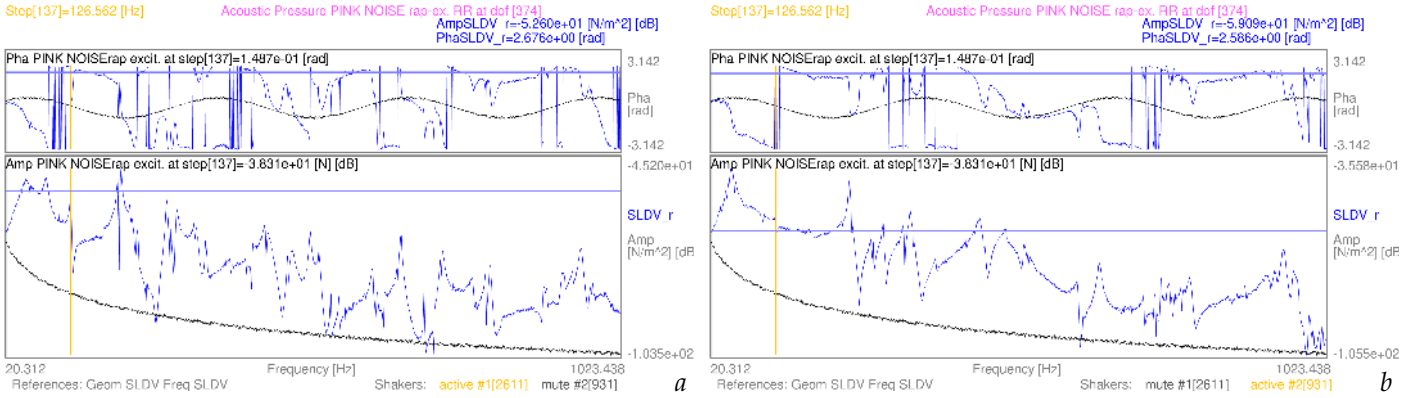

Figure 7. SLDV-based examples of *acoustic pressure complex-valued spectrum* graphs in the frequency domain evaluated in acoustic dof 374, from a *pink noise-rap* excitation, by shaker 1 in (*a*), shaker 2 in (*b*).

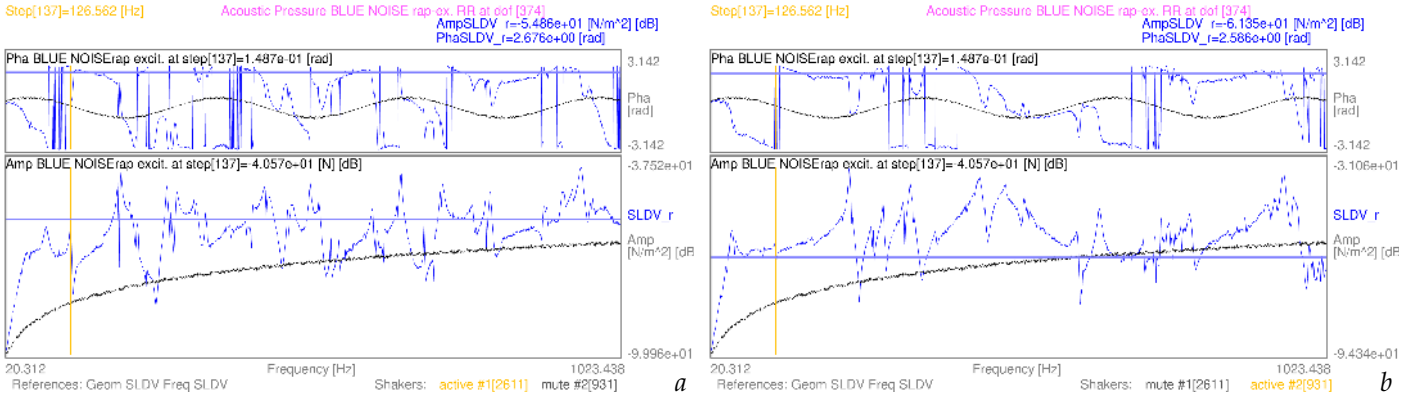

Figure 8. SLDV-based examples of *acoustic pressure complex-valued spectrum* graphs in the frequency domain evaluated in acoustic dof 374, from a *blue noise-rap* excitation, by shaker 1 in (*a*), shaker 2 in (*b*).

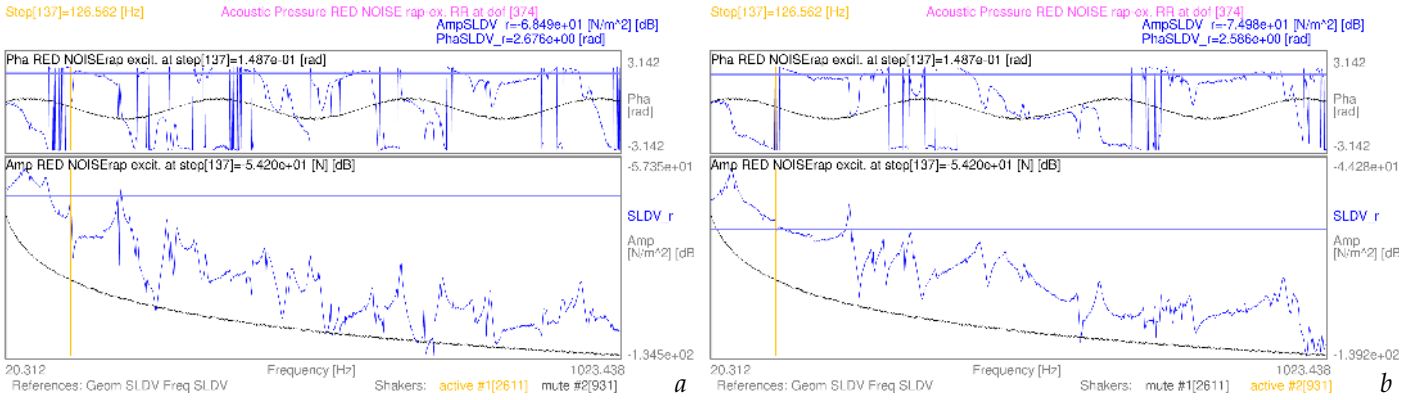

Figure 9. SLDV-based examples of *acoustic pressure complex-valued spectrum* graphs in the frequency domain evaluated in acoustic dof 374, from a *red noise-rap* excitation, by shaker 1 in (*a*), shaker 2 in (*b*).

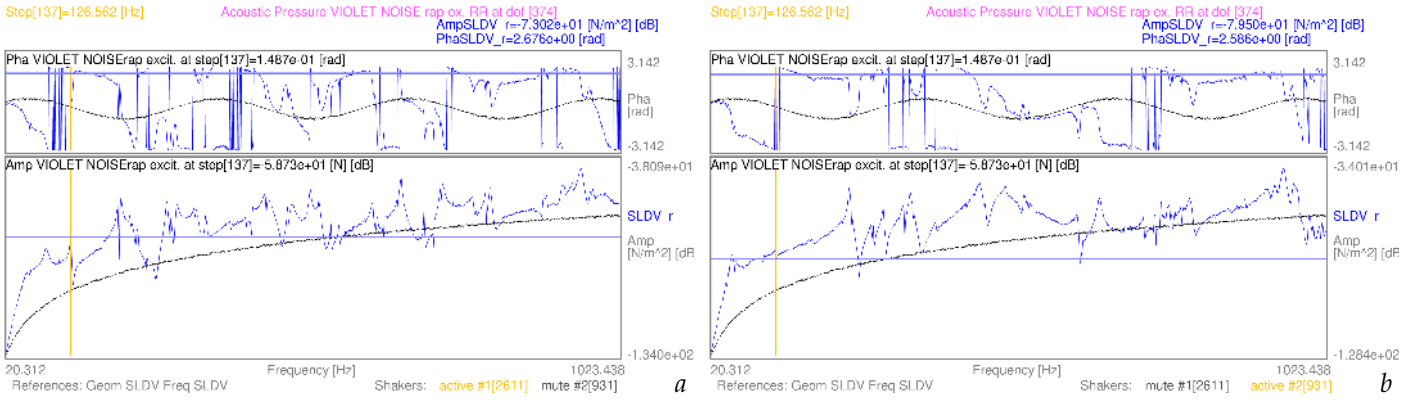

Figure 10. SLDV-based examples of *acoustic pressure complex-valued spectrum* graphs in the frequency domain evaluated in acoustic dof 374, from a *violet noise-rap* excitation, by shaker 1 in (*a*), shaker 2 in (*b*).

introduces a moderate variability of the scaling, as can be appreciated in Figure 6, appearing as a limited increase in thickness of the amplitude uncertainties in both the black and blue functions. Instead, the chosen $\theta(\omega)$ function – with its parameters and a scattering up to $\pm 12.5\%$ – determines the marked *complex phase* variabilities.

With the other noise colours, instead, the *complex amplitude* modulation given by each excitation becomes self-evident, with clear repercussions on the *acoustic pressures* from the original shapes of the *vibro-acoustic transfer matrix*, recalled from Figure 3. Besides, the *complex phase* variabilities replicate what commented above for the *white noise-rap* excitation, the phase parameters remaining exactly the same. The *pink noise-rap* excitation gives in both tiles of Figure 7 a moderate (in logarithmic scale) decrease of the *complex amplitudes* in the acoustic pressure spectra. With an opposite effect, the *blue noise-rap* excitation raises moderately the higher frequency contributions of the *complex amplitudes* in the *acoustic pressure* in Figure 8. The stronger descent of the *complex amplitudes* is due to the *red noise-rap* excitation in Figure 9. Specular effect is contributed to the *complex amplitudes* of $p(\boldsymbol{a}_a, \omega)$ by the *violet noise-rap* excitation in Figure 10.

3.4. Airborne Acoustic-Vibrational FRFs from Experiment-Based SLDV Mobilities

Following the formulation of Equation (10), the *pseudo-inverse vibro-acoustic FRFs* $\boldsymbol{V}_{f\boldsymbol{a}}^{+}(\omega)$ (or *acoustic-vibrational FRF matrix*) of force over airborne sound pressures can be achieved, as shown in the single *pseudo-inverse vibro-acoustic FRF* of Figure 11, where the airborne pressure field is considered acting on the single acoustic dof 374 and the force in the structural dof 2611 of shaker 1 in tile *a*, in the structural dof 931 of shaker 2 in

tile b. The same can be repeated for all the N_a=2601 acoustic dofs in the acoustic mesh. The comparison between the *vibro-acoustic transfer matrix* of Figure 3 and the *acoustic-vibrational transfer matrix* of Figure 11 is straightforward: there is a clear reflection of all the *complex-valued* data parts, without distortions. How the whole *complex-valued* information is retained in the pseudo-inversion, up to the numerical precision of the routines, can be clearly appreciated. The successful evaluation of the *pseudo-inverse vibro-acoustic FRFs* $\boldsymbol{V}_{fa}^{+}(\omega)$ plays, therefore, a crucial role in the following force retrieval from airborne acoustic fields.

3.5. Airborne Structural Force Evaluation as Induced by Known Pressure Fields

For the identification of the force $\hat{F}_{S1}(\omega)$ in the structural dof 2611 of shaker 1 (f = 2611 = $S1$), or $\hat{F}_{S2}(\omega)$ in the structural dof 931 of shaker 2 (f = 931 = $S2$), by means of Equation (9), the whole airborne pressure field acting on all the N_a dofs of the acoustic mesh must be used, together with all the corresponding *pseudo-inverse vibro-acoustic FRFs* in Section 3.4. The *coloured noise* excitation, in the "rap" variations, on shakers 1–2 was adopted to simulate the pressure fields with the different *complex amplitude* modulations and selected phasing modifications in the whole frequency range of interest.

In Figure 12*a* the nearly-even *white noise-rap* excitation $F(\omega)$ (in black) – with ±6.25% of amplitude scattering around the value of 7.500e-02 N and sinusoidal phase lag with ±12.5% scattering around the sine magnitude of 0.75 rad in the whole frequency domain – and the identified force $\hat{F}_{S1}(\omega)$ (in blue) are shown together. Apparently, the functions are completely superimposed in Figure 12*a*, where the ranges are adapted to the actual functions; however, the truncation of the values at the 3rd decimal can not highlight tiny discrepancies. Instead, as summarised in the second and third columns of Tables 4–5 for the errors in the *complex amplitudes* and *complex phases*, the punctual values tell the very small difference between the original excitation and the identified one, close to computational[10] precision, which only Figure 12*b* can reveal by displaying the differences evaluated by Equation (11) against the functions' ranges (fourth and fifth columns of Tables 4–5).

The same considerations can be made about the *white noise-rap* excitation $F(\omega)$ when acting on shaker 2, with the retrieved force $\hat{F}_{S2}(\omega)$ in Figure 17*a*, and with the errors $Err_{F_{S2}}(\omega)$ in Figure 17*b*. Tables 4–5 are useful to summarise the ranges, in the *complex amplitudes* and *complex phases*, of both the retrieval errors and the forces.

[10] The custom C-language/OpenMP computational engine, written by the author, exploits the 64-bit machine computational precision (see [69]) for `double` floating numbers, or machine epsilon of $2^{-52} \approx 2.220e{-}16$.

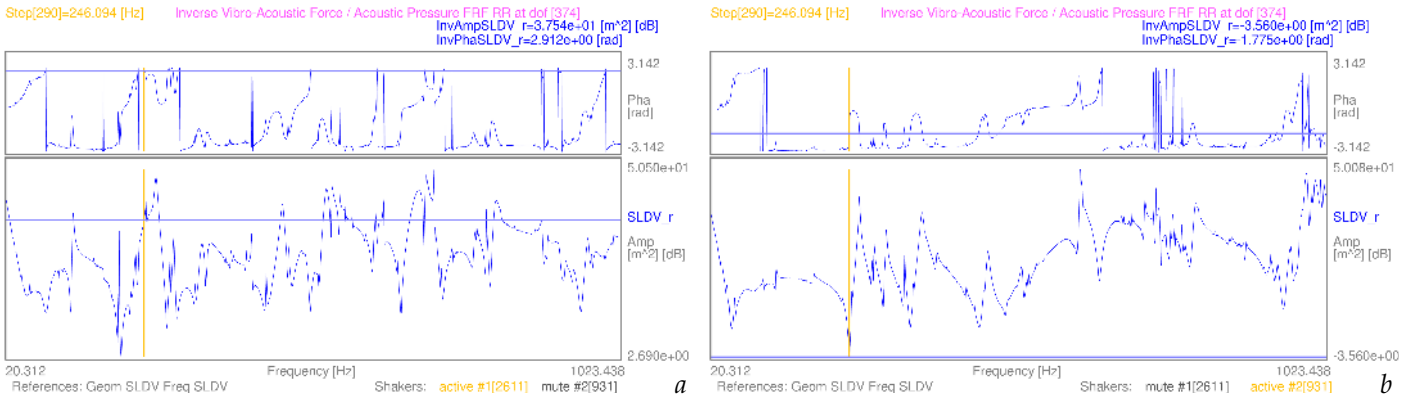

Figure 11. SLDV-based examples of *inverse vibro-acoustic FRF* graphs in the frequency domain evaluated as force in shaker 1 (structural dof 2611) in (*a*), in shaker 2 (structural dof 931) in (*b*), over the airborne acoustic pressure from dof 374.

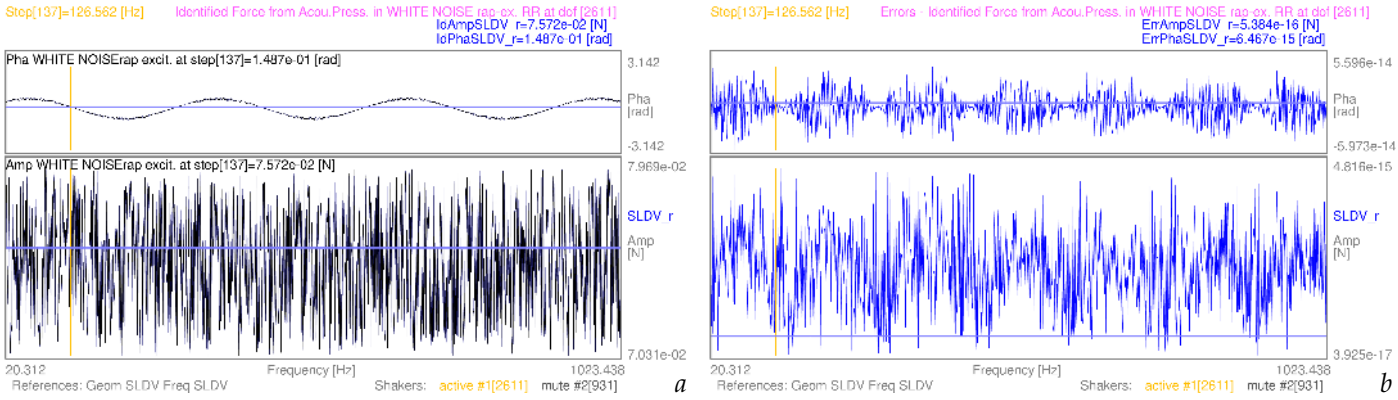

Figure 12. SLDV-based example of *identified force complex-valued spectrum* graph in (*a*), and related errors in (*b*), in the frequency domain evaluated as *white noise-rap* force in shaker 1 from the whole airborne acoustic pressure field.

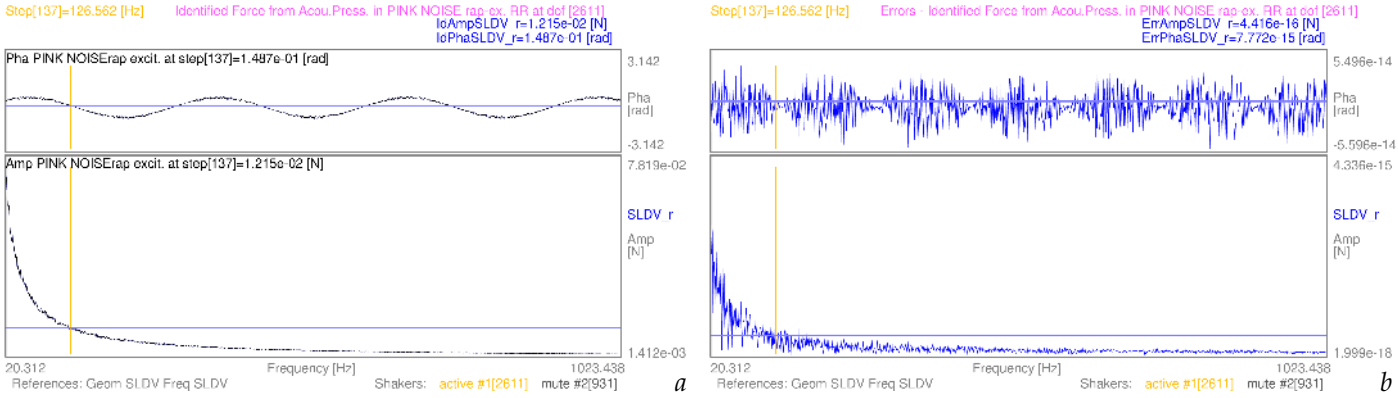

Figure 13. SLDV-based example of *identified force complex-valued spectrum* graph in (*a*), and related errors in (*b*), in the frequency domain evaluated as *pink noise-rap* force in shaker 1 from the whole airborne acoustic pressure field.

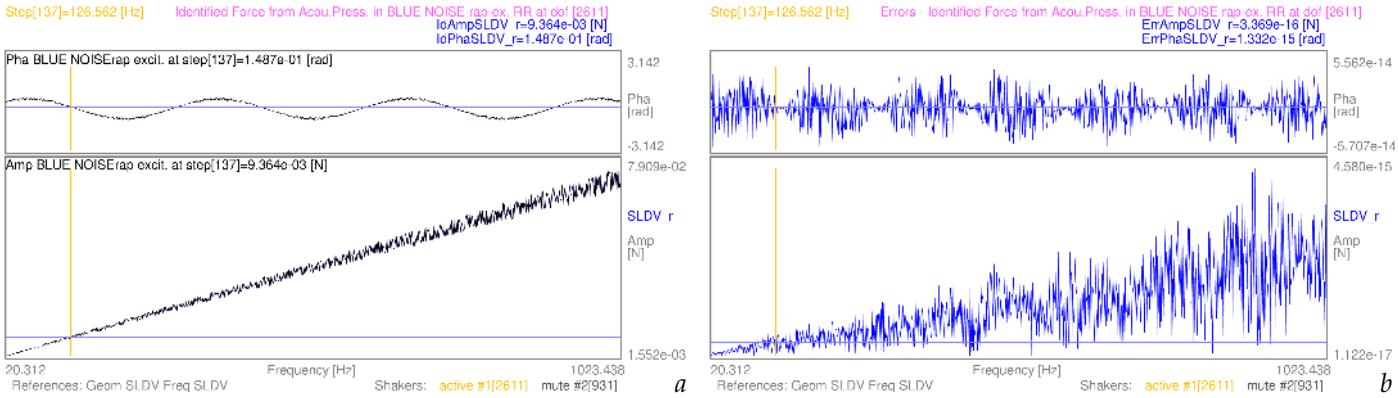

Figure 14. SLDV-based example of *identified force complex-valued spectrum* graph in (*a*), and related errors in (*b*), in the frequency domain evaluated as *blue noise-rap* force in shaker 1 from the whole airborne acoustic pressure field.

In Figure 13*a* the original *pink noise-rap* excitation $F(\omega)$ (in black) – with the *complex amplitude* and *phase* contaminated by the random variations in the whole frequency domain – and the identified force $\hat{F}_{S1}(\omega)$ (in blue) are shown together, again totally superimposed, because in Figure 13*a* the precision is truncated only at the 3rd decimal in the punctual values, while the ranges are now orders of magnitude greater than the real difference between the curves. Also in this case, only from Equation (11) – depicted in Figure 13*b* – can the right information be drawn. However, it is clear how the magnitude of the functions

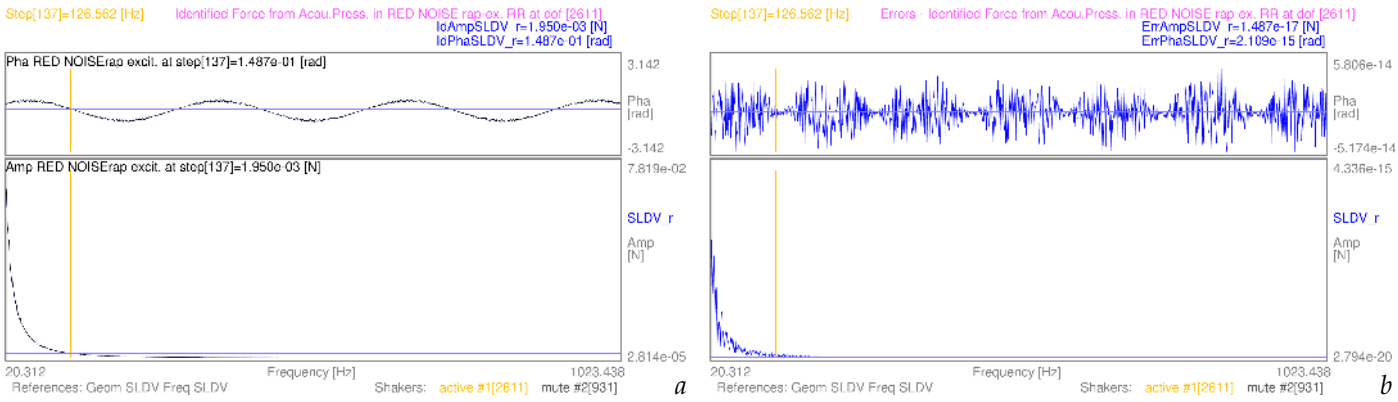

Figure 15. SLDV-based example of *identified force complex-valued spectrum* graph in (*a*), and related errors in (*b*), in the frequency domain evaluated as *red noise-rap* force in shaker 1 from the whole airborne acoustic pressure field.

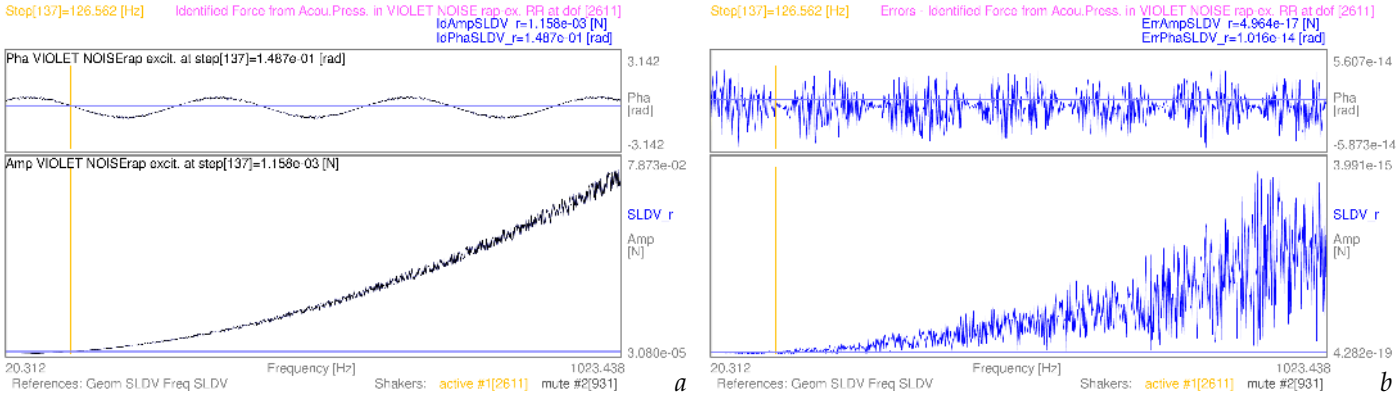

Figure 16. SLDV-based example of *identified force complex-valued spectrum* graph in (*a*), and related errors in (*b*), in the frequency domain evaluated as *violet noise-rap* force in shaker 1 from the whole airborne acoustic pressure field.

expands the error ranges of both the *complex amplitude* and *complex phase*. The example of $\hat{F}_{S2}(\omega)$ force retrieval, in the chain due to the original *pink noise-rap* excitation $F(\omega)$ in shaker 2, is sketched in Figures 18*a*-18*b*, with the extreme values as reported in Tables 4–5.

The retrieval of the original *blue noise-rap* excitation $F(\omega)$ in shaker 1, with related errors, is sketched in the tiles of Figure 14, while the same is made in Figure 19 for shaker 2 excitation, with minimal variations in the values of Tables 4–5.

Similar deployment of the original *red noise-rap* excitation $F(\omega)$ in shaker 1 is made in the tiles of Figure 15, instead in Figure 20 for shaker 2 excitation.

Finally, the original *violet noise-rap* excitation $F(\omega)$ in shaker 1, and its retrieved $\hat{F}(\omega)$, are shown in the tiles of Figure 16, while the same excitation in shaker 2 is shown in Figure 21, with the same approach and similar conclusions on the values of Tables 4–5, which gather the data about all the excitations of these simulations.

4. Discussion

Section 3 has clearly shown how this simplified experiment-based approach – fully formulated in Section 2 – can simulate the *direct* and *pseudo-inverse vibro-acoustic* problems of flat surfaces. In particular, as clearly deployed in Section 3.2, the augmented detail – coming from full-field datasets – gives an unprecedented mapping continuity in the *complex-valued* blending by the Green's functions in the diffusion matrix of Equation (5) to obtain the *vibro-acoustic transfer matrix* $\boldsymbol{V}_{af}(\omega)$, with no sacrifice for the experiment-based structural dynamics underneath. The latter, instead, enriches the simulations by extracting

the real-life behaviour of the set-up realisation. Note that the measurement errors enter in the estimation of the full-field *mobilities* at the core of the approach, therefore strong care must be paid during the testing. This is even more important for SLDV, here used, which proved (see [40,53]) to suffer from hardly distinguishable scanning-related faults, which can ruin the whole mapping, while the *native/image-based* full field technologies have a better continuity in the spatial domain. Although simplified, this achievement deserves attention, also because it can be used to raise the benchmarks in purely numerical simulations, and to let them assess better when their models need better and refined updating or tuning.

Section 3.3 has shown clearly how the *complex-valued* formulation of the whole approach is fundamental to retain the whole structural dynamics in the broad frequency band spectra of the *acoustic pressure* $p(\boldsymbol{a}_a, \omega)$ simulations, while changing the *complex-valued* excitation spectrum. This accurate formulation can clearly work with any measured force from real testing, again with no assumptions, except for the respect of the linearity, under which the full-field *mobilities* were estimated. But in the case a new excitation level is needed, in a recursive manner, new *mobilities* must be acquired to make the approach valid.

Section 3.4 has shown, in this simplified – but mathematically sound and rigorous for the *complex-valued* formulation widely adopted – approach, how effective can the *pseudo-inverse* be. For the shake of compactness, the *acoustic-vibrational FRF* $\boldsymbol{V}_{f\boldsymbol{a}}^{+}(\omega)$ in Equation (10) was evaluated only between the one acoustic dof and the two structural dofs of the shakers here used, to make the appropriate comparison with the function already shown for the *direct* problem of the *vibro-acoustic transfer matrix* $\boldsymbol{V}_{\boldsymbol{af}}(\omega)$. Nonetheless, the

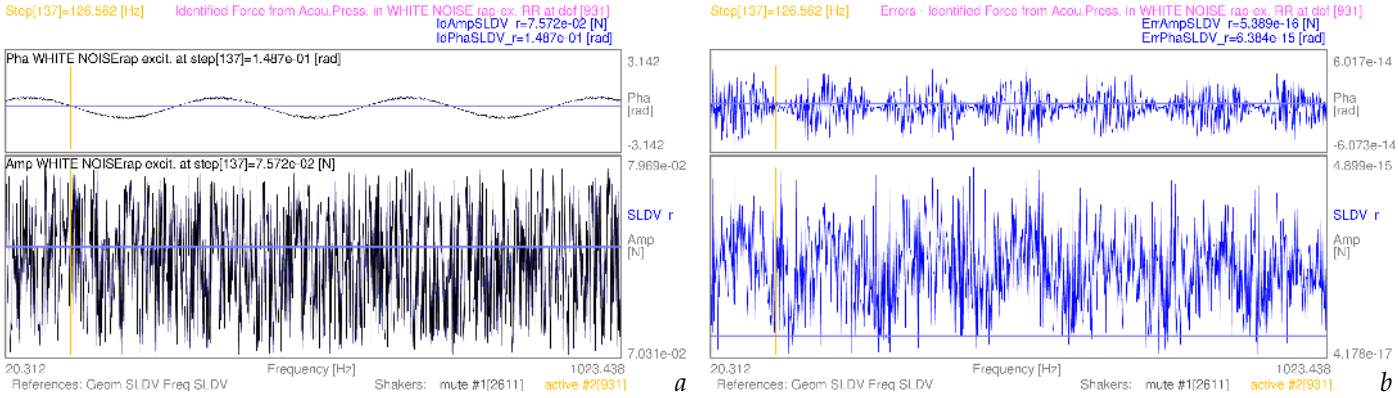

Figure 17. SLDV-based example of *identified force complex-valued spectrum* graph in (*a*), and related errors in (*b*), in the frequency domain evaluated as *white noise-rap* force in shaker 2 from the whole airborne acoustic pressure field.

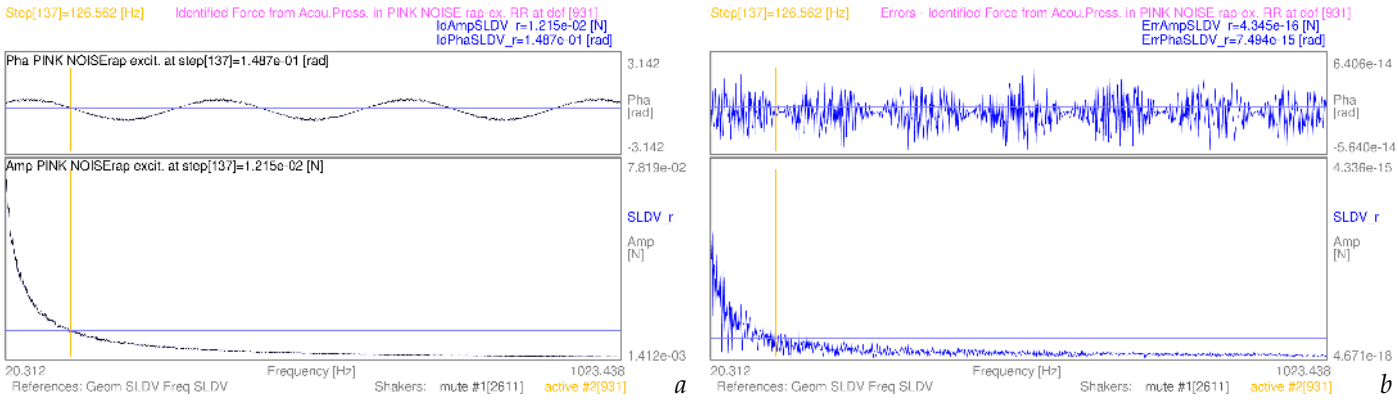

Figure 18. SLDV-based example of *identified force complex-valued spectrum* graph in (*a*), and related errors in (*b*), in the frequency domain evaluated as *pink noise-rap* force in shaker 2 from the whole airborne acoustic pressure field.

pseudo-inversion worked well with no computational distortions, therefore the quality of the SLDV-based *mobilities* is again of uttermost importance, as the biggest errors may come from a sub-optimal testing campaign, rather than from rounds-off in the approach.

Section 3.5 has revealed the high precision of the approach, by means of the $\boldsymbol{V}_{fa}^{+}(\omega)$ and the *acoustic pressure fields* evaluated in the *direct vibro-acoustic* problem, in reconstructing the original excitation force, in all its *complex-valued* spectrum, again with no simplifications, except for linearity, as quoted above. While looking at Table 4, the distribution of the

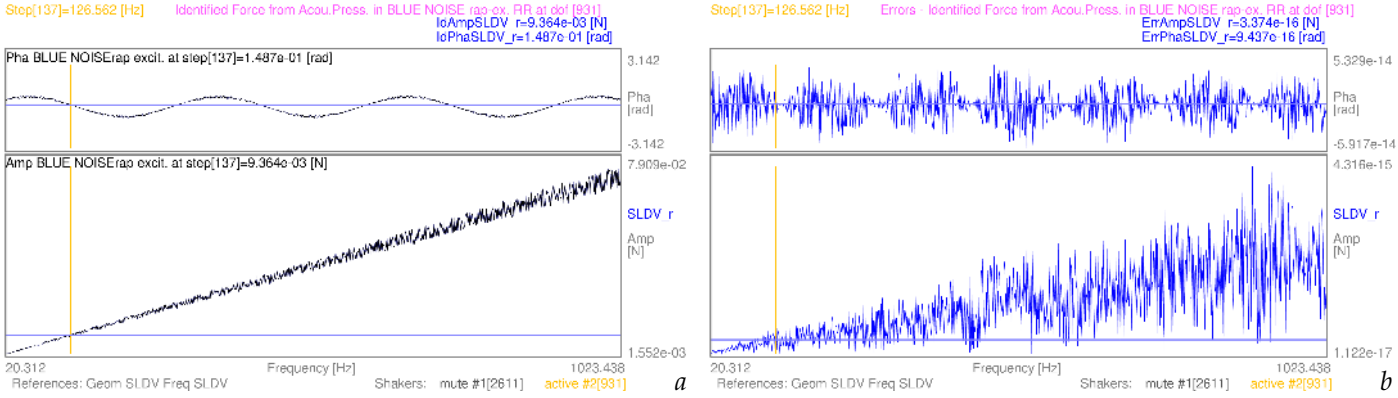

Figure 19. SLDV-based example of *identified force complex-valued spectrum* graph in (*a*), and related errors in (*b*), in the frequency domain evaluated as *blue noise-rap* force in shaker 2 from the whole airborne acoustic pressure field.

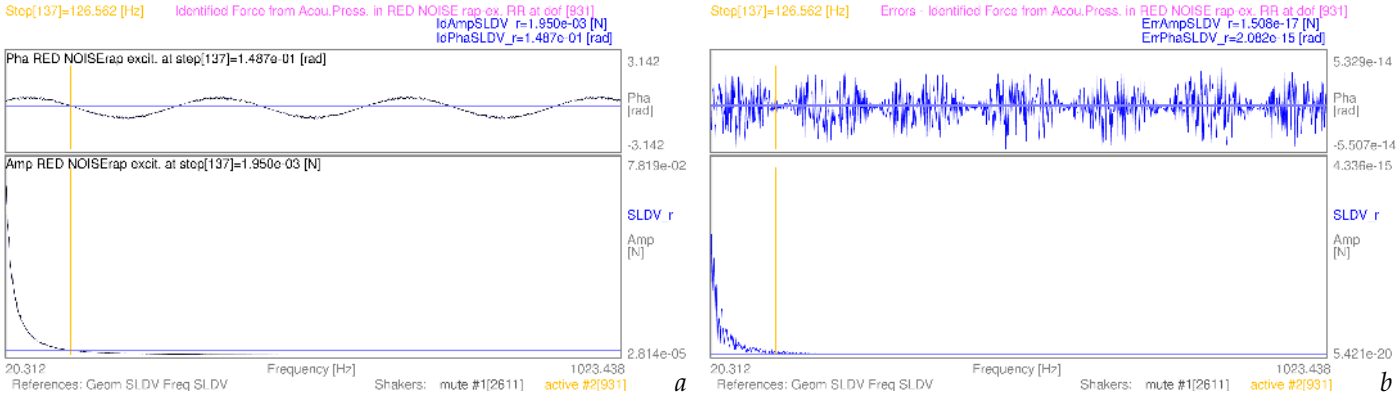

Figure 20. SLDV-based example of *identified force complex-valued spectrum* graph in (*a*), and related errors in (*b*), in the frequency domain evaluated as *red noise-rap* force in shaker 2 from the whole airborne acoustic pressure field.

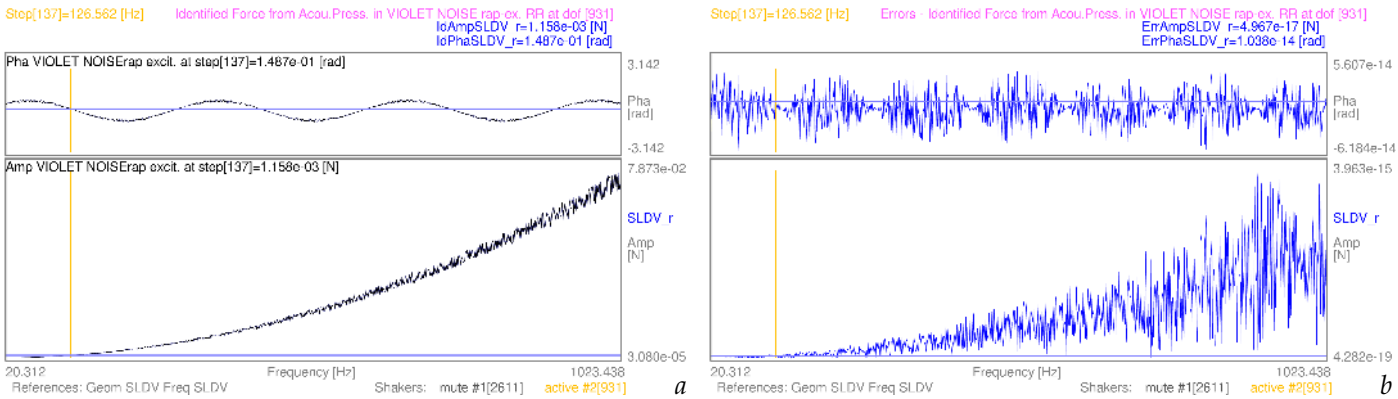

Figure 21. SLDV-based example of *identified force complex-valued spectrum* graph in (*a*), and related errors in (*b*), in the frequency domain evaluated as *violet noise-rap* force in shaker 2 from the whole airborne acoustic pressure field.

errors in the 10 examples of Section 3.5 seems broader and linked to the colour of the noise, especially regarding the second column, the one with the lower bound of the amplitude errors. Indeed, the range for it is a bit broader than expected ([2.794e-20, 4.178e-17] N), but always of many orders lower than the reference amplitude F_0 of 7.500e-02 N, or than the values in the fourth and fifth column of Table 4. The upper bound of the identification errors is more compressed for all the simulated initial excitations, specifically in the range of [3.963e-15,4.899e-15] N in the third column of Table 4. Thus, in the ten simulated examples, the errors of the *complex amplitude* of the identified force stay in the wide range of [2.794e-20, 4.899e-15]. But, if one normalises them against the extremes of the *complex amplitudes* of each function, as in the sixth and seventh column of Table 4, the relative errors result more constrained, independently of the excitation case, in a tighter range of [5.582e-16, 6.148e-14].

Instead, Table 5 just reports variations in the *complex phase* due to the random function evaluations in the adopted sinusoidal phase descriptor – common to all the signals, with the widest range in [-6.184e-14, 6.406e-14]. When the normalisation is made against the extremes of the *complex phase* wrapping ($\pm\pi$ rad), the relative phase errors stay therefore in a very similarly bounded range of [-1.901e-14, 2.039e-14].

Fusing together the extremes of these relative errors, the computational relative error of the identification approach in the *pseudo-inversion* of Equation (10) has a maximum of 6.148e-14, which can be considered remarkably low and close to the 64-bit machine- and numerical data-storage- precisions, especially if the thousands of parallel operations involved in the airborne force identification approach[11] are taken into account. In [55], the relative errors of the amplitude were in the range [1.402e-14, 2.207e-14] with *pure white noise* excitation, without random variations nor phasing, at a lower amplitude of 1.0e-02 N and 0.1 m of distance between the acoustic mesh and the plate, but from the reduced DIC dataset, interpolated to SLDV references, again with $N_q = 2907$ structural dofs and of $N_a = 2601$ acoustic dofs. In [54], the relative error range had the widest extremes in [3.391e-20, 1.018e-14], but from *raw* DIC datasets and excitation at a lower amplitude of 5.0e-02 N and 0.2 m of distance between the acoustic mesh and the plate. Such accurate results were obtained from *raw* DIC-based datasets with the contributions of $N_q = 11988$ structural dofs and of $N_a = 10201$ acoustic dofs, with all the *complex-valued* computation involved.

Which role is played by the distance – between the structural domain and the acoustic mesh – on the accuracy of the whole approach should be more investigated, as well as which role is played by the number of dofs in both the acoustic and the structural domains. But, of much greater relevance, remains the quality of the measurements for estimating the *receptances* or the *mobilities*, which are responsible of sensing the real-life structural dynamics of the actual realisation of the set-up. Therefore, the clear lesson learned is to invest an expert's time in the set-up preparation/tuning and resources in a high-quality measurement campaign (here, around 3.36 days just for each SLDV-*mobilities*' scanning), because the proposed approach proved to be very accurate and very computationally fast (here around only 1 minute, in the parallel computing custom coding), but it is not designed to correct the potential issues of the initial test measurements.

[11] The dataset used – 1285 frequency lines, 2601 acoustic dofs, 2907 structural dofs – for each simulation needed the peak allocation of 145.7 GB of RAM, accessed simultaneously by 24 logical threads in parallel OpenMP-based computing in the custom C-language code, `gcc 7.5.0 target:x86_64-suse-linux` in OpenSUSE® Linux environment with `kernel 6.4`, and on a workstation with 192 GB of RAM, 12 physical cores in dual hexacore Intel® Xeon® X5690 CPUs running at 3.46–3.73 GHz. After the data loading, the *vibro-acoustic transfer matrix* $\boldsymbol{V}_{af}(\omega)$ was computed in around 35 s, while the successive evaluations of the *acoustic-vibrational FRF* $\boldsymbol{V}_{fa}^{+}(\omega)$, of the airborne force $\hat{F}(\omega)$ and relative errors took around 21 s.

Table 4. Summary of the computational errors in the *complex amplitude* of force identification from airborne acoustic pressure fields.

Noise Colour + Shaker	Min Amp Err [N]	Max Amp Err [N]	Min Amp [N]	Max Amp [N]	Min Amp Err / Min Amp	Max Amp Err / Max Amp
white-rap S1	3.925e-17	4.816e-15	7.031e-02	7.969e-02	5.582e-16	6.043e-14
white-rap S2	4.178e-17	4.899e-15	7.031e-02	7.969e-02	5.942e-16	6.148e-14
pink-rap S1	1.999e-18	4.336e-15	1.412e-03	7.819e-02	1.416e-15	5.545e-14
pink-rap S2	4.671e-18	4.336e-15	1.412e-03	7.819e-02	3.308e-15	5.545e-14
blue-rap S1	1.122e-17	4.580e-15	1.552e-03	7.909e-02	7.229e-15	5.791e-14
blue-rap S2	1.122e-17	4.316e-15	1.552e-03	7.909e-02	7.229e-15	5.457e-14
red-rap S1	2.794e-20	4.336e-15	2.814e-05	7.819e-02	9.929e-16	5.545e-14
red-rap S2	5.421e-20	4.336e-15	2.814e-05	7.819e-02	1.926e-15	5.545e-14
violet-rap S1	4.282e-19	3.991e-15	3.080e-05	7.873e-02	1.390e-14	5.069e-14
violet-rap S2	4.282e-19	3.963e-15	3.080e-05	7.873e-02	1.390e-14	5.034e-14

Table 5. Summary of the computational errors in the *complex phase* of force identification from airborne acoustic pressure fields.

Noise Colour + Shaker	Min Pha Err [rad]	Max Pha Err [rad]	Min Pha [rad]	Max Pha [rad]	Min Pha Err / Min Pha	Max Pha Err / Max Pha
white-rap S1	-5.973e-14	5.596e-14	$-\pi$	$+\pi$	-1.901e-14	1.781e-14
white-rap S2	-6.073e-14	6.017e-14	$-\pi$	$+\pi$	-1.933e-14	1.915e-14
pink-rap S1	-5.596e-14	5.496e-14	$-\pi$	$+\pi$	-1.781e-14	1.749e-14
pink-rap S2	-5.640e-14	6.406e-14	$-\pi$	$+\pi$	-1.795e-14	2.039e-14
blue-rap S1	-5.707e-14	5.562e-14	$-\pi$	$+\pi$	-1.817e-14	1.770e-14
blue-rap S2	-5.917e-14	5.329e-14	$-\pi$	$+\pi$	-1.883e-14	1.696e-14
red-rap S1	-5.174e-14	5.806e-14	$-\pi$	$+\pi$	-1.647e-14	1.848e-14
red-rap S2	-5.507e-14	5.329e-14	$-\pi$	$+\pi$	-1.753e-14	1.696e-14
violet-rap S1	-5.873e-14	5.607e-14	$-\pi$	$+\pi$	-1.869e-14	1.785e-14
violet-rap S2	-6.184e-14	5.607e-14	$-\pi$	$+\pi$	-1.968e-14	1.785e-14

5. Conclusions

The *complex-valued* formulation of the *direct* and the *pseudo-inverse vibro-acoustic* problem, by means of the simplification of the Rayleigh integral approximation, has here proved to be accurate and computationally fast also for the use of SLDV-based *mobilities*, which – in some cases – have shown some unexpected noise from scanning-related issues.

The experiment-based full-field *mobilities* permitted to fully retain, with high quality mapping in the spatial and frequency domains, the structural dynamics of the actual realisation of the testing set-up, when evaluating *vibro-acoustic transfer matrices* and *pressure fields*, with no further assumptions nor simplifications, except for linearity. They become a valid alternative for those cases in which a purely numerical model of a complex structural dynamics cannot be easily tuned; at the same time, new benchmarks for synthetic digital-twins can be set. The procedure to retrieve an *airborne force* – impressed by *airborne pressure fields* on the flexible flat surface – proved to be reliable also with SLDV-based *mobilities*, as extensively documented by the different simulated examples.

The quality of the obtained methodological achievements fosters future investigations on more complex vibrating structures, also coupled with different fluids, for NVH and reliability studies, together with further experimental evidences from real-life challenging environments.

Funding: TEFFMA project ended in 2015; no further specific funding was received afterwards.

Data Availability Statement: Data are contained within the article.

Acknowledgments: This activity is a spin-off of the Project TEFFMA (Towards Experimental Full Field Modal Analysis), funded by the European Commission at the Technische Universitaet Wien, through the Marie Curie FP7-PEOPLE-IEF-2011 PIEF-GA-2011-298543 grant, for which the Research Executive Agency is greatly acknowledged. TU-Wien, in the person of Prof. Johann Wassermann and his staff, are kindly acknowledged for having hosted the TEFFMA project of the author at the *Schwingungs- und Strukturanalyse* / Optical Vibration Measurement Laboratory. The workstation used to extensively process the datasets in the custom code was provided by the author on his own savings. Professor Roberta Mullini is wholeheartedly acknowledged for her care in the English proofreading of the text.

Conflicts of Interest: The author declares no conflicts of interest.

Abbreviations

The following abbreviations are used in this manuscript:

DIC	Digital image correlation
dof	Degree of freedom
EFFMA	Experimental full-field modal analysis
EMA	Experimental modal analysis
ESPI	Electronic speckle pattern interferometry
FRF	Frequency response function
NAH	Nearfield Acoustic Holography
NDT	Non-destructive testing
NVH	Noise and vibration harshness
ODS	Operative deflection shape
SLDV	Scanning laser Doppler vibrometer
(ω)	Circular frequency dependency
$\dot{\mathbf{X}}(\omega)$	Velocity map
$\mathbf{F}(\omega)$	Excitation force
$\mathbf{H_v}(\omega)$	*Mobility* map
$\boldsymbol{V_{af}}(\omega)$	Vibro-Acoustic FRFs
$\boldsymbol{p}(\boldsymbol{a_a}, \omega)$	Sound Pressure Fields mapping
$\boldsymbol{V_{fa}^{+}}(\omega)$	Pseudo-Inverse Vibro-Acoustic or Acoustic-Vibrational FRFs
$\hat{F}_f(\omega)$	Identified Airborne Force
$\boldsymbol{bold}$	Bold characters for array notation

References

1. Maynard, J.D.; Williams, E.G.; Lee, Y. Nearfield acoustic holography: I. Theory of generalized holography and the development of NAH. *J. Acoust. Soc. Am.* **1985**, *78*, 1395–1413. https://doi.org/10.1121/1.392911.
2. Veronesi, W.A.; Maynard, J.D. Nearfield acoustic holography (NAH) II. Holographic reconstruction algorithms and computer implementation. *J. Acoust. Soc. Am.* **1987**, *81*, 1307–1322. https://doi.org/10.1121/1.394536.
3. Williams, E.G. *Fourier Acoustics: Sound Radiation and Nearfield Acoustical Holography*; Elsevier Science: Amsterdam, The Netherlands, 1999. https://doi.org/10.1016/B978-0-12-753960-7.X5000-1.
4. Kirkup, S. Computational solution of the acoustic field surrounding a baffled panel by the Rayleigh integral method. *Appl. Math. Model.* **1994**, *18*, 403–407. https://doi.org/10.1016/0307-904X(94)90227-5.
5. Gérard, F.; Tournour, M.; Masri, N.; Cremers, L.; Felice, M.; Selmane, A. Acoustic transfer vectors for numerical modeling of engine noise. *Sound Vib.* **2002**, *36*, 20–25.
6. Fahy, F. *Foundations of Engineering Acoustics*; Academic Press: London, UK, 2003; pp. 1–443. https://doi.org/10.1016/B978-0-12-247665-5.X5000-0.
7. Desmet, W. Boundary Element Method in Acoustics. Technical Report, Katholieke Universiteit Leuven, Belgium, Mechanical Engineering Department, Noise & Vibration Research Group, 2004, for the ISAAC 15-Course on Numerical and Applied Acoustics.
8. Kirkup, S.; Thompson, A. Computing the Acoustic Field of a Radiating Cavity by the Boundary Element-Rayleigh Integral Method (BERIM). In Proceedings of the World Congress on Engineering, WCE 2007, London, UK, 2–4 July 2007; Ao, S.I., Gelman,

L., Hukins, D.W.L., Hunter, A., Korsunsky, A.M., Eds.; Lecture Notes in Engineering and Computer Science; Newswood Limited: Hong Kong, China, 2007; pp. 1401–1406.
9. Arenas, J.P. Numerical computation of the sound radiation from a planar baffled vibrating surface. *J. Comput. Acoust.* **2008**, *16*, 321–341. https://doi.org/10.1142/S0218396X08003671.
10. Arunkumar, M.; Pitchaimani, J.; Gangadharan, K.; Leninbabu, M. Vibro-acoustic response and sound transmission loss characteristics of truss core sandwich panel filled with foam. *Aerosp. Sci. Technol.* **2018**, *78*, 1–11. https://doi.org/10.1016/j.ast.2018.03.029.
11. Kirkup, S. The Boundary Element Method in Acoustics: A Survey. *Appl. Sci.* **2019**, *9*, 1642. https://doi.org/10.3390/app9081642.
12. Lesoinne, M.; Sarkis, M.; Hetmaniuk, U.; Farhat, C. A linearized method for the frequency analysis of three-dimensional fluid/structure interaction problems in all flow regimes. *Comput. Methods Appl. Mech. Eng.* **2001**, *190*, 3121–3146, in *Advances in Computational Methods for Fluid-Structure Interaction*, https://doi.org/10.1016/S0045-7825(00)00385-6.
13. Sandberg, G.; Wernberg, P.A.; Davidsson, P. Fundamentals of Fluid-Structure Interaction. In *Computational Aspects of Structural Acoustics and Vibration*; Springer Vienna, Austria, 2009; Volume 505, Chapter 2, pp. 23–101. https://doi.org/10.1007/978-3-211-89651-8_2.
14. Ohayon, R.; Soize, C. Advanced computational dissipative structural acoustics and fluid-structure interaction in low- and medium-frequency domains. Reduced-order models and uncertainty quantification. *Int. J. Aeronaut. Space Sci.* **2012**, *13*, 127–153. https://doi.org/10.5139/IJASS.2012.13.2.127.
15. Vicente, W.; Picelli, R.; Pavanello, R.; Xie, Y. Topology optimization of frequency responses of fluid-structure interaction systems. *Finite Elem. Anal. Des.* **2015**, *98*, 1–13. https://doi.org/10.1016/j.finel.2015.01.009.
16. Zhou, Q.; Li, D.-f.; Da Ronch, A.; Chen, G.; Li, Y.-m. Computational fluid dynamics-based transonic flutter suppression with control delay. *J. Fluids Struct.* **2016**, *66*, 183–206. https://doi.org/10.1016/j.jfluidstructs.2016.07.002.
17. Dowell, E.H.; Hall, K.C. Modeling of Fluid-Structure Interaction. *Annu. Rev. Fluid Mech.* **2001**, *33*, 445–490. https://doi.org/https://doi.org/10.1146/annurev.fluid.33.1.445.
18. Kamakoti, R.; Shyy, W. Fluid-structure interaction for aeroelastic applications. *Prog. Aerosp. Sci.* **2004**, *40*, 535–558. https://doi.org/10.1016/j.paerosci.2005.01.001.
19. Werter, N.; De Breuker, R. A novel dynamic aeroelastic framework for aeroelastic tailoring and structural optimisation. *Compos. Struct.* **2016**, *158*, 369–386. https://doi.org/10.1016/j.compstruct.2016.09.044.
20. Li, D.; Zhou, Q.; Chen, G.; Li, Y. Structural dynamic reanalysis method for transonic aeroelastic analysis with global structural modifications. *J. Fluids Struct.* **2017**, *74*, 306–320. https://doi.org/10.1016/j.jfluidstructs.2017.06.004.
21. Li, D.; Da Ronch, A.; Chen, G.; Li, Y. Aeroelastic global structural optimization using an efficient CFD-based reduced order model. *Aerosp. Sci. Technol.* **2019**, *94*, 105354. https://doi.org/10.1016/j.ast.2019.105354.
22. Chen, Z.; Zhao, Y.; Huang, R. Parametric reduced-order modeling of unsteady aerodynamics for hypersonic vehicles. *Aerosp. Sci. Technol.* **2019**, *87*, 1–14. https://doi.org/10.1016/j.ast.2019.01.035.
23. Tian, W.; Gu, Y.; Liu, H.; Wang, X.; Yang, Z.; Li, Y.; Li, P. Nonlinear aeroservoelastic analysis of a supersonic aircraft with control fin free-play by component mode synthesis technique. *J. Sound Vib.* **2021**, *493*, 115835. https://doi.org/10.1016/j.jsv.2020.115835.
24. Wang, X.; Yang, Z.; Zhou, S.; Zhang, G. Complex damping influences on the oscillatory/static instability characteristics of heated panels in supersonic airflow. *Mech. Syst. Signal Process.* **2022**, *165*, 108369. https://doi.org/10.1016/j.ymssp.2021.108369.
25. Patil, H.H.; Pitchaimani, J. Sound radiation characteristics of a beam under supersonic airflow and non-uniform temperature field. *Aerosp. Sci. Technol.* **2024**, *147*, 109001. https://doi.org/10.1016/j.ast.2024.109001.
26. Heylen, W.; Lammens, S.; Sas, P. *Modal Analysis Theory and Testing*, 2nd ed.; Katholieke Universiteit Leuven: Leuven, Belgium, 1998. ISBN 90-73802-61-X.
27. Ewins, D.J. *Modal Testing-Theory, Practice and Application*, 2nd ed.; Research Studies Press Ltd.: Baldock, UK, 2000; p. 400. ISBN 978-0-86380-218-8.
28. Van der Auweraer, H.; Dierckx, B.; Haberstok, C.; Freymann, R.; Vanlanduit, S. Structural modelling of car panels using holographic modal analysis. In Proceedings of the 1999 Noise and Vibration Conference, Traverse City, MI, USA, 17 May 1999; Volume 3, pp. 1495–1506, SAE P-342. https://doi.org/10.4271/1999-01-1849.
29. Van der Auweraer, H.; Steinbichler, H.; Haberstok, C.; Freymann, R.; Storer, D. Integration of pulsed-laser ESPI with spatial domain modal analysis: Results from the SALOME project. In Proceedings of the 4th International Conference on Vibration Measurements by Laser Techniques: Advances and Applications, Ancona, Italy, 20–23 June 2000; SPIE: Bellingham, WA, USA, 2000; Volume 4072, pp. 313–322. https://doi.org/10.1117/12.386741.
30. Van der Auweraer, H.; Steinbichler, H.; Haberstok, C.; Freymann, R.; Storer, D.; Linet, V. Industrial Applications of Pulsed-laser ESPI vibration analysis. In Proceedings of the XIX IMAC, Kissimmee, FL, USA. SEM, 5–8 February 2001; pp. 490–496.
31. Van der Auweraer, H.; Steinbichler, H.; Vanlanduit, S.; Haberstok, C.; Freymann, R.; Storer, D.; Linet, V. Application of stroboscopic and pulsed-laser electronic speckle pattern interferometry (ESPI) to modal analysis problems. *Meas. Sci. Technol.* **2002**, *13*, 451–463. https://doi.org/10.1088/0957-0233/13/4/305.

32. Zanarini, A. Broad frequency band full field measurements for advanced applications: Point-wise comparisons between optical technologies. *Mech. Syst. Signal Process.* **2018**, *98*, 968–999. https://doi.org/10.1016/j.ymssp.2017.05.035.
33. Zanarini, A. Competing optical instruments for the estimation of Full Field FRFs. *Measurement* **2019**, *140*, 100–119. https://doi.org/10.1016/j.measurement.2018.12.017.
34. Zanarini, A. Full field optical measurements in experimental modal analysis and model updating. *J. Sound Vib.* **2019**, *442*, 817–842. https://doi.org/10.1016/j.jsv.2018.09.048.
35. Baqersad, J.; Poozesh, P.; Niezrecki, C.; Avitabile, P. Photogrammetry and optical methods in structural dynamics – A review. *Mech. Syst. Signal Process.* **2017**, *86*, 17–34, in SI: *Full-field, non-contact vibration measurement methods: comparisons and applications*. https://doi.org/10.1016/j.ymssp.2016.02.011.
36. Wang, W.; Mottershead, J.E.; Ihle, A.; Siebert, T.; Schubach, H.R. Finite element model updating from full-field vibration measurement using digital image correlation. *J. Sound Vib.* **2011**, *330*, 1599–1620. https://doi.org/10.1016/j.jsv.2010.10.036.
37. Wang, W.; Mottershead, J.; Siebert, T.; Pipino, A. Frequency response functions of shape features from full-field vibration measurements using digital image correlation. *Mech. Syst. Signal Process.* **2011**, *28*, 333–347. https://doi.org/10.1016/j.ymssp.2011.11.023.
38. LeBlanc, B.; Niezrecki, C.; Avitabile, P.; Sherwood, J.; Chen, J. Surface Stitching of a Wind Turbine Blade Using Digital Image Correlation. In *Topics in Modal Analysis II, Proceedings of the 30th IMAC, A Conference on Structural Dynamics, SEM*; Allemang, R., De Clerck, J., Niezrecki, C., Blough, J., Eds.; Springer: New York, NY, USA, 2012; Volume 6, pp. 277–284. https://doi.org/10.1007/978-1-4614-2419-2_27.
39. Ehrhardt, D.A.; Allen, M.S.; Yang, S.; Beberniss, T.J. Full-field linear and nonlinear measurements using Continuous-Scan Laser Doppler Vibrometry and high speed three-dimensional Digital Image Correlation. *Mech. Syst. Signal Process.* **2017**, *86*, 82–97. https://doi.org/10.1016/j.ymssp.2015.12.003.
40. Zanarini, A. On the making of precise comparisons with optical full field technologies in NVH. In Proceedings of the ISMA2020 Including USD2020 – International Conference on Noise and Vibration Engineering, Leuven, Belgium, 7–9 September 2020; pp. 2293–2308, in Vol. *Optical methods and computer vision for vibration engineering*.
41. Liu, W.; Ewins, D. The Importance Assessment of RDOF in FRF Coupling Analysis. In Proceedings of the IMAC 17th Conference, Kissimmee, FL, USA, 8–11 February 1999; Society for Experimental Mechanics (SEM): Bethel, CT, USA, 1999; pp. 1481–1487.
42. Research Network. *QUATTRO Brite-Euram Project no: BE 97-4184*; Technical Report, European Commision Research Framework Programs: Brussels, Belgium, 1998.
43. Friswell, M.; Mottershead, J.E. *Finite Element Model Updating in Structural Dynamics*; Solid Mechanics and Its Applications; Kuwler Academic Publishers & Springer Science+Business Media, Dordrecht, Netherlands, 1995; p. 292. ISBN 978-0-7923-3431-6.
44. Haeussler, M.; Klaassen, S.; Rixen, D. Experimental twelve degree of freedom rubber isolator models for use in substructuring assemblies. *J. Sound Vib.* **2020**, *474*, 115253. https://doi.org/10.1016/j.jsv.2020.115253.
45. Zanarini, A. Chasing the high-resolution mapping of rotational and strain FRFs as receptance processing from different full-field optical measuring technologies. *Mech. Syst. Signal Process.* **2022**, *166*, 108428. https://doi.org/10.1016/j.ymssp.2021.108428.
46. Zanarini, A. Introducing the concept of defect tolerance by fatigue spectral methods based on full-field frequency response function testing and dynamic excitation signature. *Int. J. Fatigue* **2022**, *165*, 107184. https://doi.org/10.1016/j.ijfatigue.2022.107184.
47. Zanarini, A. About the excitation dependency of risk tolerance mapping in dynamically loaded structures. In Proceedings of the ISMA2022 Including USD2022 – International Conference on Noise and Vibration Engineering, Leuven, Belgium, 12–14 September 2022; pp. 3804–3818, in Vol. *Structural Health Monitoring*.
48. Zanarini, A. Risk Tolerance Mapping in Dynamically Loaded Structures as Excitation Dependency by Means of Full-Field Receptances. In Proceedings of the IMAC XLI-International Modal Analysis Conference-Keeping IMAC Weird: Traditional and Non-Traditional Applications of Structural Dynamics, Austin, TX, USA, 13–16 February 2023; chapter 9, in Baqersad, J., Di Maio, D. (eds.); Springer Nature AG: Cham, Switzerland & SEM Society for Experimental Mechanics: Bethel, CT, USA, 2023; *Computer Vision & Laser Vibrometry*, Volume 6, pp. 43–56. https://doi.org/10.1007/978-3-031-34910-2_9.
49. Zanarini, A. Exploiting DIC-based full-field receptances in mapping the defect acceptance for dynamically loaded components. *Procedia Struct. Integr.* **2024**, *54C*, 99–106, Proceedings of The 5th International Conference on Structural Integrity, 28 August – 1 September, 2023. https://doi.org/10.1016/j.prostr.2024.01.061.
50. Zanarini, A. Mapping the defect acceptance for dynamically loaded components by exploiting DIC-based full-field receptances. *Eng. Fail. Anal.* **2024**, *163*, 108385. https://doi.org/10.1016/j.engfailanal.2024.108385.
51. Zanarini, A. On the approximation of sound radiation by means of experiment-based optical full-field receptances. In Proceedings of the ISMA2022 Including USD2022 – International Conference on Noise and Vibration Engineering, Leuven, Belgium, 12–14 September 2022; pp. 2735–2749, in Vol. *Optical Methods*.
52. Zanarini, A. Experiment-based Optical Full-field receptances in the Approximation of Sound Radiation from a Vibrating Plate. In Proceedings of the IMAC XLI-International Modal Analysis Conference-Keeping IMAC Weird: Traditional and Non-Traditional

Applications of Structural Dynamics, Austin, TX, USA, 13–16 February 2023; chapter 4, in Baqersad, J., Di Maio, D. (eds.); Springer Nature AG: Cham, Switzerland & SEM Society for Experimental Mechanics: Bethel, CT, USA, 2023; *Computer Vision & Laser Vibrometry*, Volume 6, pp. 1–13. https://doi.org/10.1007/978-3-031-34910-2_4.

53. Zanarini, A. On the influence of scattered errors over full-field receptances in the Rayleigh integral approximation of sound radiation from a vibrating plate. *Acoustics* **2023**, *5*, 948–986. https://doi.org/10.3390/acoustics5040055.
54. Zanarini, A. Assessing the retrieval procedure of complex-valued forces from airborne pressure fields by means of DIC-based full-field receptances in simplified pseudo-inverse vibro-acoustics. *Aerosp. Sci. Technol.* **2024**, *157*, 109757. https://doi.org/10.1016/j.ast.2024.109757.
55. Zanarini, A. On the use of full-field receptances in inverse vibro-acoustics for airborne structural dynamics. *Procedia Struct. Integr.* **2024**, *54C*, 107–114, Proceedings of The 5th International Conference on Structural Integrity, 28 August – 1 September, 2023. https://doi.org/10.1016/j.prostr.2024.01.062.
56. Kreis, T. *Handbook of Holographic Interferometry: Optical and Digital Methods*; Wiley-VCH: Berlin, Germany, 2004. https://doi.org/10.1002/3527604154.
57. Wind, J.; Wijnant, Y.; de Boer, A. Fast evaluation of the Rayleigh integral and applications to inverse acoustics. In Proceedings of the ICSV13, the Thirteenth International Congress on Sound and Vibration, Vienna, Austria, 2–6 July 2006; International Institute of Acoustics and Vibration (IIAV): Auburn, AL, USA, 2006; pp. 1–8.
58. Michel Tournour, L.C.; Guisset, P.; Augusztinovicz, F.; Marki, F. Inverse Numerical Acoustics Based on Acoustic Transfer Vectors. In Proceedings of the 7th International Congress on Sound and Vibration – ICSV7, Garmisch-Partenkirchen, Germany, 4–7 July 2000; pp. 2069–2076.
59. Citarella, R.; Federico, L.; Cicatiello, A. Modal acoustic transfer vector approach in a FEM-BEM vibro-acoustic analysis. *Eng. Anal. Bound. Elem.* **2007**, *31*, 248–258. https://doi.org/10.1016/j.enganabound.2006.09.004.
60. Guillaume, P.; Parloo, E.; De Sitter, G. Source identification from noisy response measurements using an iterative weighted pseudo-inverse approach. In Proceedings of the 2002 International Conference on Noise and Vibration Engineering, ISMA, Heverlee, Belgium, 16–18 September 2002; pp. 1817–1824.
61. Vanlanduit, S.; Guillaume, P.; Cauberghe, B.; Parloo, E.; De Sitter, G.; Verboven, P. On-line identification of operational loads using exogenous inputs. *J. Sound Vib.* **2005**, *285*, 267–279. https://doi.org/10.1016/j.jsv.2004.08.028.
62. Mas, P.; Sas, P. Acoustic Source Identification Based on Microphone Array Processing. Technical Report, Katholieke Universiteit Leuven, Belgium, Mechanical Engineering Department, Noise & Vibration Research Group, 2004, for the ISAAC 15-Course on Numerical and Applied Acoustics.
63. Khoo, S.; Ismail, Z.; Kong, K.; Ong, Z.; Noroozi, S.; Chong, W.; Rahman, A. Impact force identification with pseudo-inverse method on a lightweight structure for under-determined, even-determined and over-determined cases. *Int. J. Impact Eng.* **2014**, *63*, 52–62. https://doi.org/10.1016/j.ijimpeng.2013.08.005.
64. Leclère, Q.; Pereira, A.; Bailly, C.; Antoni, J.; Picard, C. A unified formalism for acoustic imaging based on microphone array measurements. *Int. J. Aeroacoustics* **2017**, *16*, 431–456. https://doi.org/10.1177/1475472X17718883.
65. Chiariotti, P.; Martarelli, M.; Castellini, P. Acoustic beamforming for noise source localization - Reviews, methodology and applications. *Mech. Syst. Signal Process.* **2019**, *120*, 422–448. https://doi.org/10.1016/j.ymssp.2018.09.019.
66. Cumbo, R.; Tamarozzi, T.; Janssens, K.; Desmet, W. Kalman-based load identification and full-field estimation analysis on industrial test case. *Mech. Syst. Signal Process.* **2019**, *117*, 771–785. https://doi.org/10.1016/j.ymssp.2018.08.045.
67. Wikipedia.org. Speed of Sound. 2024. Available online: https://en.wikipedia.org/wiki/Speed_of_sound (accessed on 2 March 2024).
68. Wikipedia.org. Density of Air. 2024. Available online: https://en.wikipedia.org/wiki/International_Standard_Atmosphere (accessed on 2 March 2024).
69. Wikipedia.org. Machine Epsilon. 2024. Available online: https://en.wikipedia.org/wiki/Machine_epsilon (accessed on 18 April 2024).